

Deep Equilibrium models for Poisson imaging inverse problems via Mirror Descent

Christian Daniele¹ Silvia Villa² Samuel Vaiter³ Luca Calatroni⁴

¹ MaLGA Center, DIBRIS, University of Genoa, Italy
`christian.daniele@edu.unige.it`

²MaLGA Center, DIIMA, University of Genoa, Italy
`silvia.villa@unige.it`

³ CNRS & Université Côte d’Azur, Laboratoire J. A. Dieudonné. Nice, France.
`samuel.vaiter@cnrs.fr`

MaLGA Center, DIBRIS, University of Genoa & MMS, Istituto Italiano di Tecnologia
(IIT), Italy
`luca.calatroni@unige.it`

Abstract

Deep Equilibrium Models (DEQs) are implicit neural networks with fixed points, which have recently gained attention for learning image regularization functionals, particularly in settings involving Gaussian fidelities, where assumptions on the forward operator ensure contractiveness of standard (proximal) Gradient Descent operators. In this work, we extend the application of DEQs to Poisson inverse problems, where the data fidelity term is more appropriately modeled by the Kullback–Leibler divergence. To this end, we introduce a novel DEQ formulation based on Mirror Descent defined in terms of a tailored non-Euclidean geometry that naturally adapts with the structure of the data term. This enables the learning of neural regularizers within a principled training framework. We derive sufficient conditions and establish refined convergence results based on the Kurdyka–Łojasiewicz framework for subanalytic functions with non-closed domains to guarantee the convergence of the learned reconstruction scheme and propose computational strategies that enable both efficient training and parameter-free inference. Numerical experiments show that our method outperforms traditional model-based approaches and it is comparable to the performance of Bregman Plug-and-Play methods, while mitigating their typical drawbacks, such as time-consuming tuning of hyper-parameters.

The code is publicly available at <https://github.com/christiandaniele/DEQ-MD>.

Keywords: Poisson inverse problems, deep equilibrium models, Mirror Descent, learned regularization, nonconvex optimization, Kurdyka–Łojasiewicz property

MSC codes: 65K10, 65J22, 94A08, 47N10

1 Introduction

Image reconstruction problems in the presence of Poisson noise arise naturally in various scientific imaging domains where the measurements are governed by photon-limited observations. Prominent examples include fluorescence microscopy [9], astronomical imaging [22], and Positron Emission Tomography [52], all of which involve scenarios where photon counts are inherently low and follow discrete statistics.

Mathematically, given dimensions $m, n \in \mathbb{N}_*$, the task is to recover an unknown non-negative image $x \in \mathbb{R}_{\geq 0}^n$ from Poisson-degraded measurements $y \in \mathbb{R}_{\geq 0}^m$, modeled as:

$$y \sim \text{Poiss}(Ax), \tag{1.1}$$

where $A \in \mathbb{R}_{\geq 0}^{m \times n}$ is a known, typically ill-posed, forward operator. The operator $\text{Pois}(\cdot)$ denotes a multidimensional Poisson distribution, where each component y_j satisfies $\mathbb{E}(y_j) = \text{Var}(y_j) = (Ax)_j$ for $j = 1, \dots, m$. We use the convention¹ $\text{Pois}(\mathbf{0}) = \mathbf{0}$, where $\mathbf{0}$ is the distribution s.t. $\mathbb{E}(\mathbf{0}) = \text{Var}(\mathbf{0}) = 0$. This indicates the case where the Poisson distribution’s parameter is 0, resulting in a degenerate Poisson distribution. Note that the formulation in (1.1) does not include an explicit background term $b \in \mathbb{R}_{> 0}^m$, which is sometimes introduced in practice to avoid degeneracy in regions of low expected intensity [28].

In comparison with standard Gaussian noise modeling, the Poisson assumption can be easily shown to correspond to a non-quadratic log-likelihood data term which is the Kullback-Leibler (KL) divergence function $\text{KL} : \mathbb{R}_{> 0}^m \times \mathbb{R}_{> 0}^m \rightarrow \mathbb{R}_{\geq 0}$ that reads:

$$\text{KL}(y, Ax) := \sum_{i=1}^m y_i \log \left(\frac{y_i}{(Ax)_i} \right) + (Ax)_i - y_i, \quad (1.2)$$

which is well-defined also for vanishing values y_j upon the convention $0 \log 0 = 0$. In this framework, to ensure that $(Ax)_i > 0$ for all $i \in \{1, \dots, m\}$, we consider a forward operator A such that its i -th row vector, a_i , satisfies $a_i \in \mathbb{R}_{> 0}^n \setminus \{0\}$ for all $i \in \{1, \dots, m\}$, and $x \in \mathbb{R}_{> 0}^n$. These conditions are not overly restrictive, for instance, a standard convolution operator typically satisfies them.

Early contributions to image reconstruction based on Kullback–Leibler (KL) divergence minimization date back to the foundational works of [39, 45, 52], which introduced iterative regularization schemes grounded in the Expectation–Maximization (EM) framework. A notable instance is the Richardson–Lucy algorithm, developed independently in [39, 45], which applies EM updates to linear image deconvolution under Poisson noise. Building on this framework, Byrne proposed in [18] the Multiplicative Algebraic Reconstruction Technique (MART), a class of iterative methods derived from cross-entropy (Kullback–Leibler) minimization using multiplicative updates under non-negativity constraints. While MART (and its simultaneous variant SMART) aim at minimizing $\text{KL}(Ax, y)$, this objective differs from the more common Poisson-likelihood divergence $\text{KL}(y, Ax)$. In this respect, the expectation-maximization maximum-likelihood (EMML) algorithm — and in particular Byrne’s accelerated block-iterative variant (RBI-EMML) as described in [19] — align more closely with the standard Poisson noise model.

While these methods remain effective and are still used in modern applications (see, e.g., [64]), they typically require early stopping to prevent overfitting to noise, which introduces a reliance on heuristic tuning to obtain satisfactory results.

To address these limitations, a wide range of model-based regularization techniques have been developed to incorporate explicit prior knowledge about the image, often in combination with smoothed variants of the KL divergence in (1.2) to enable standard gradient-based optimization. A common strategy involves introducing a small background term [28], resulting in the modified fidelity $\text{KL}(y, Ax + b)$, which is twice continuously differentiable on the non-negative orthant. To ensure non-negativity of the reconstruction, projected Gradient Descent and its scaled or preconditioned variants have been explored [17]. In parallel, more structured priors such as sparsity-promoting ℓ_1 -norm penalties [22, 24], total variation (TV) [51], and higher-order variants [21] have been successfully employed. These models are typically optimized using (accelerated) proximal gradient algorithms [16, 44] or primal–dual methods [20], often incorporating advanced features such as variable metric scaling, inexact proximal steps, and stochastic updates to improve convergence and computational efficiency.

Directly minimizing the KL divergence in (1.2) without adding a background smoothing term poses significant algorithmic challenges. Although the functional $\text{KL}(y, A \cdot)$ is differentiable on

¹This choice is motivated by the property that for a sequence of random variables $\{X_n\}_{n \in \mathbb{N}}$ with $X_n \sim \text{Pois}(\lambda_n)$, if $\lambda_n \rightarrow 0$ as $n \rightarrow \infty$, then $X_n \xrightarrow{d} \mathbf{0}$, where \xrightarrow{d} denotes convergence in distribution.

$\mathbb{R}_{>0}^n$, its gradient is not Lipschitz continuous therein due to the singularity near zero. This prevents the straightforward application of standard (proximal) gradient algorithms. To overcome this, Bregman-type optimization methods—such as those developed in [6, 15, 56]—relax the need for Lipschitz-smoothness and naturally accommodate domain constraints, for instance, non-negativity. A prominent example is Mirror Descent (MD) [42], whose convergence properties can be studied under a non-Euclidean analogue of L -smoothness, defined relative to a strictly convex function h that specifies the underlying geometry. In the context of Poisson inverse problems, this notion of relative smoothness amounts to the existence of a constant $L > 0$ such that the function $Lh - \text{KL}(y, A \cdot)$ is convex [6, 15, 38]. For the KL divergence, this condition is satisfied by choosing h as Burg’s entropy, defined by $h(x) = -\sum_{i=1}^n \log(x_i)$. Based on this choice, one can construct Bregman (proximal) gradient operators using the associated Bregman distance, leading to optimization schemes that share strong analogies with the multiplicative updates found in EM and MART algorithms.

Leveraging the connection between optimization algorithms and deep learning, we propose a novel approach to Poisson inverse problems based on the MD iteration interpreted as the recurrent core of a deep equilibrium model (DEQ). Our goal is to learn image regularization functionals in a principled and convergent manner—without requiring proximal operators or contractiveness of classical descent schemes. This builds upon the broader idea of using optimization-inspired architectures in image reconstruction. Among them, algorithm unrolling [1, 41] treats each iteration of an algorithm as a trainable neural layer, while Plug-and-Play (PnP) methods [31, 40, 58] replace proximal steps with learned Gaussian denoisers, often interpreted through Tweedie’s formula [34]. Variants such as RED [47], contractive network models [54, 55, 57], and Bregman-PnP approaches [2, 29] offer convergence guarantees under various assumptions. In particular, [29] analyzes convergence in the Poisson setting using relative smoothness and suitable training upon inverse Gamma noise statistics, while [33] introduces a mirror-Langevin sampler tailored to Poisson likelihoods, handling non-negativity and lack of L -smoothness without any Gaussian smoothing.

Our approach departs from these by embedding Mirror Descent within a DEQ framework. While DEQs have been previously studied under Gaussian fidelities using contractive operators such as (proximal) Gradient Descent or ADMM [26], their extension to the non-Euclidean and non-contractive MD case with a deep, non-convex regularization functional remains unexplored. This is precisely the focus of our work: providing a convergent and trainable formulation of DEQs for Poisson inverse problems grounded in Bregman geometry, enabling a fully implicit and less sensitive to parameters tuning scheme w.r.t. to PnP approaches.

Contribution This work introduces a novel DEQ framework for solving linear Poisson inverse problems in imaging by learning regularization functionals directly from data. We begin in Section 2 by recalling the general DEQ formulation and its interpretation as a fixed-point iteration. In Section 3, we propose a DEQ architecture built upon Mirror Descent (MD), specifically tailored to minimize the Kullback–Leibler divergence (1.2). This choice allows us to bypass the standard L -smoothness assumption by instead relying on a relative smoothness condition with respect to a non-Euclidean geometry.

Section 4 presents our main theoretical contribution: despite the lack of strong convexity of the KL divergence and without any convexity assumption on the learnable regularization functional, we derive sufficient conditions to guarantee convergence of the proposed fixed-point DEQ-MD reconstruction scheme. To this end, we extend the result [11, Theorem 3.1] on the validity of the Kurdyka–Łojasiewicz property to subanalytic functions with not-necessarily closed domain. This is indeed a crucial property which allows us to extend existing DEQ analyses beyond strongly convex data fidelities and contractive operators.

Implementation-related aspects are discussed in Sections 5 and 6, where we address the

computational challenges associated with both the forward and backward passes of the fixed-point layer. These include, for instance, backtracking strategies for step-size selection and Jacobian-free strategies for efficient and memory-saving training.

Finally, in Section 7, we validate our approach on several imaging tasks. Numerical results show improved reconstruction quality over classical model-based methods and competitive performance compared to recent Bregman-PnP algorithms, while offering a less complex architecture, reduced sensitivity to hyper-parameter tuning, and full parameter-freedom at inference time, provided the level of noise in the image is known at test time. As an outlook, some encouraging numerical tests addressing generalization properties (to different tasks and to different noise models than the one used during training) are reported. Section 8 contains some concluding remarks and perspectives.

For the sake of readability, detailed technical definitions and results are deferred to Appendix A, whereas the main statements and principal results are presented in the main body of the paper.

2 Deep Equilibrium Models (DEQs)

In this section, we provide a self-contained introduction to DEQs [5]. Roughly speaking, they can be defined as infinite-depth neural networks with fixed points. More precisely, a DEQ is defined by considering a single operator layer $f_\theta : X \subseteq \mathbb{R}^n \rightarrow X$. A DEQ can be viewed as the infinite composition of f_θ , where the same parameters $\theta \in \Theta \subset \mathbb{R}^D$ are reused at each step (a property known as weight tying). The operator f_θ thus serves as the fundamental building block of a DEQ and can itself be implemented as a neural network. Equivalently, a DEQ can be interpreted as the fixed point operator that maps each input x^0 to one of the fixed points of the DEQ-layer f_θ . To make these notions more precise, we will study the convergence properties of DEQs in terms of existence of fixed points for f_θ . To this end, we introduce the following notion of well-posedness.

Definition 2.1 (Well-posedness of a DEQ). *Let $X \subset \mathbb{R}^n$ be an open set and let $f_\theta : X \rightarrow X$ with $\theta \in \Theta \subset \mathbb{R}^D$ be a DEQ layer. We say that the DEQ associated with f_θ is well-posed if:*

1. *The set of fixed points $\text{Fix}(f_\theta) = \{x^\infty \in X : f_\theta(x^\infty) = x^\infty\} \neq \emptyset$;*
2. *For all initialization points $x^0 \in X$, the sequence $\{x^k\}_{k \in \mathbb{N}}$, defined by*

$$x^k := \begin{cases} x^0 & \text{if } k = 0 \\ f_\theta(x^{k-1}) & \text{if } k > 0, \end{cases}$$

converges to $x^\infty \in \text{Fix}(f_\theta)$.

Designing a well-posed DEQ means constructing an operator $f_\theta : X \rightarrow X$ that admits at least one fixed point and ensures convergence of its associated iteration. A class of operators which defines naturally a well-posed DEQ is the set of contractive operators, which ensures both existence and uniqueness of the fixed point as well as convergence of fixed point iteration schemes.

2.1 DEQs for image reconstruction

In the context of image reconstruction, given a noisy measurement $y \in \mathbb{R}^m$, the goal is to design a DEQ layer $f_\theta(\cdot; y)$ such that its fixed points $x^\infty = f_\theta(x^\infty; y)$ provides a good approximation of the unknown ground truth x .

When f_θ is parameterized by a neural network, training a DEQ thus amounts to learning the weights θ that minimize the reconstruction error. Note that since $f_\theta(\cdot; y)$ maps the input space

to itself, computing one of its fixed point requires an initial guess $x^0 \in \mathbb{R}^n$, which can typically be chosen as a simple function of y , such as $x^0 = A^\top y$. While convergence is ensured under strong assumptions like contractiveness (see [26] and Section 2.1.1), the choice of x^0 becomes critical in more general settings where multiple fixed points may exist. Differently from contractive networks, which are independent on the choice of the initialization, this choice becomes critical in settings where multiple fixed points may exist. Note, however, that enforcing a network to be a contraction may limit its expressivity.

To formalize the DEQ training procedure, consider a dataset of image pairs $\{(x_i^*, y_i)\}_{i=1}^n$, where each $x_i^* \in \mathbb{R}^n$ is a ground truth image and $y_i \in \mathbb{R}^m$ is its corresponding degraded and noisy observation. The goal is to learn parameters $\hat{\theta} \in \Theta$ such that

$$\hat{\theta} \in \operatorname{argmin}_{\theta \in \Theta} \mathcal{L}(\theta) := \frac{1}{n} \sum_{i=1}^n \ell(x^\infty(\theta; y_i, x_i^0), x_i^*), \quad (2.1)$$

where $x_i^0 \in \mathbb{R}^n$ is the i -th initialization, $x^\infty(\theta; y_i, x_i^0) \in \operatorname{Fix}(f_\theta(\cdot; y_i))$ is the limit of the fixed point iteration in Definition 2.1, and $\ell : \mathbb{R}^n \times \mathbb{R}^n \rightarrow \mathbb{R}_{\geq 0}$ is a differentiable loss function (e.g., the square loss). In the following, we describe how the existence of such fixed points can be guaranteed, and how they can be computed in practice. We emphasize that the DEQ model is used here in a specific way. The main objective is to learn the solution map of an inverse problem, mapping noisy measurements to the ground truth. This is achieved through the composition: $y \mapsto f_\theta(\cdot; y) \mapsto x^\infty(\theta; y, x^0)$.

2.1.1 Gaussian case, DE-GRAD

A simple example of f_θ arises from the formulation of a classical regularized inverse problem under additive white Gaussian noise, which reads:

$$\operatorname{argmin}_{x \in \mathbb{R}^n} \frac{1}{2} \|Ax - y\|_2^2 + \lambda R(x), \quad (2.2)$$

where $A \in \mathbb{R}^{n \times n}$ is a square matrix, $R : \mathbb{R}^n \rightarrow \mathbb{R}_{\geq 0}$ is a L -smooth regularization functional, and $\lambda > 0$ is a regularization parameter. In [26], the authors considered a DEQ model, based on applying the gradient descent algorithm to solve (2.2). The iteration reads:

$$x^{k+1} = x^k - \tau A^\top (Ax^k - y) - \tau \lambda \nabla R(x^k),$$

for a suitable step size $\tau > 0$.

To define the operator $f_\theta(\cdot; y) : \mathbb{R}^n \rightarrow \mathbb{R}^n$, the authors replaced the regularization term $\lambda \nabla R$ with a neural network $r_\theta : \mathbb{R}^n \rightarrow \mathbb{R}^n$, yielding:

$$f_\theta(x; y) := x - \tau A^\top (Ax - y) - \tau r_\theta(x). \quad (2.3)$$

Here, the regularization parameter is implicitly encoded in r_θ , and the weights of f_θ are shared with those of r_θ .

To ensure well-posedness of (2.3), the authors imposed conditions on r_θ and A to guarantee that f_θ is a contraction, which ensures existence and uniqueness of a fixed point. In particular, if the operator $r_\theta - \operatorname{Id}$ is Lipschitz-continuous with sufficiently small Lipschitz constant, then f_θ becomes a contraction [26, Theorem 1]. This result relies on the fact that the data fidelity term $\|Ax - y\|_2^2$ is strongly convex when A is injective. However, injectivity is often not satisfied in practical inverse problems, such as downsampling or inpainting, where A is typically rank-deficient. Moreover, when the data fidelity term is no longer quadratic – as in the case of the Kullback–Leibler divergence (1.2) – standard strong convexity arguments no longer apply, and more sophisticated algorithmic strategies and theoretical analyses are required to establish

convergence guarantees. In this spirit, the authors in [63] introduced a DEQ framework for Gaussian problems where convergence guarantees are established without relying on contraction properties, but based on fully optimization-based arguments. Building on this idea, we consider, in the following, optimization algorithms tailored to minimize the Kullback–Leibler divergence, and we derive fixed-point convergence results by leveraging the theoretical foundations of the underlying optimization algorithm.

3 Poisson case, Deep Equilibrium Mirror Descent (DEQ-MD)

Following [26], we leverage an optimization algorithm well-suited to the minimization of KL (1.2) to be used as a building block of a DEQ strategy. Note that such functional is constrained over the non-negative orthant and is not L -smooth, thus classical optimization schemes (e.g. Proximal Gradient Descent) do not apply in a straightforward manner.

3.1 Bregman Proximal Gradient Descent

In this section and for the following analysis, given $S \subset \mathbb{R}^n$, we will use the notation $\text{int}(S)$ and \bar{S} to indicate, respectively, its interior and its closure. The Bregman Proximal Gradient (BPG) algorithm [6, 15, 42] combined with generalized notions of smoothness, has been widely used in the literature to go beyond standard convergence assumptions of first-order optimization schemes. This algorithm can be seen as a generalization of Proximal Gradient Descent under a different geometry, potentially non-Euclidean, naturally encoding domain constraints and allowing for a weaker notion of smoothness. In more detail, given:

- a convex function $f : \mathbb{R}^n \rightarrow \mathbb{R} \cup \{+\infty\}$, differentiable on the interior of its domain,
- a proper, convex and lower semicontinuous (l.s.c.) function $\mathcal{R} : \mathbb{R}^n \rightarrow \mathbb{R} \cup \{+\infty\}$,
- a Legendre function A.3 $h : \mathbb{R}^n \rightarrow \mathbb{R} \cup \{+\infty\}$,

for $k \geq 0$, and $x^0 \in \text{int}(\text{dom}(h))$, the BPG iteration can be written as:

$$x^{k+1} = \underset{x \in \mathbb{R}^n}{\text{argmin}} \mathcal{R}(x) + \langle x - x^k, \nabla f(x^k) \rangle + \frac{1}{\tau} D_h(x, x^k), \quad (3.1)$$

where D_h is the Bregman divergence associated with h defined in A.4 and $\tau > 0$ is the step-size. Under certain compatibility conditions between f, \mathcal{R} and h [6, Lemma 2]), it is possible to get an explicit formulation of (3.1), which reads:

$$x^{k+1} = \text{Prox}_{\tau \mathcal{R}}^h(\nabla h^*(\nabla h(x^k) - \tau \nabla f(x^k))),$$

where h^* denotes the Fenchel conjugate [46] of the function h for which there holds $\nabla h^* = (\nabla h)^{-1}$ on $\text{int}(\text{dom}(h^*))$ and $\text{Prox}_{\tau \mathcal{R}}^h$ is the Bregman proximal operator of \mathcal{R} w.r.t. h , defined in A.5. The choice of the Bregman potential function h is crucial and it is related to the functional we aim to minimize. In the case of the KL divergence (1.2), a tailored choice for h is the so-called Burg’s entropy [6]:

$$h(x) = - \sum_{i=1}^n \log(x_i), \quad (3.2)$$

which enforces naturally the positivity of the desired solution. In this particular case and assuming that $R_\theta : \mathbb{R}^n \rightarrow \mathbb{R}$ is a regularization functional parameterized in terms of a differentiable neural network with weights $\theta \in \Theta$, we consider the following operator as the underlying DEQ layer:

$$f_\theta(x; y) := \Pi_{[0, a]^n}(\nabla h^*(\nabla h(x) - \tau(\nabla \text{KL}(y, Ax) + \nabla R_\theta(x))), \quad (\text{DEQ-MD})$$

where h is the Burg's entropy defined in (3.2), $a > 0$ and $\Pi_{[0,a]^n}$ denotes the projection operator on $[0, a]^n$. Note that (DEQ-MD) corresponds to a step of BPG minimizing a composite functional $\Psi : \mathbb{R}^n \rightarrow \mathbb{R} \cup \{+\infty\}$ defined by:

$$\Psi(x) := \text{KL}(y, Ax) + R_\theta(x) + \iota_{[0,a]^n}(x). \quad (3.3)$$

Due to the presence of R_θ and the indicator function $\iota_{[0,a]^n}$, the functional in (3.3) is non-convex and non-smooth. Such an indicator function is required for technical reasons which will be clarified in the following. In the case where non-smoothness is present only in the form of an indicator function ι_C of a closed and convex set $C \subset \text{dom}(h)$, BPG corresponds to a Projected Mirror Descent². For this reason, with some abuse of language, we name the proposed approach Deep Equilibrium Mirror Descent and refer to it as DEQ-MD in the following.

Note, that we decided to parameterize directly the regularization function and not its gradient as in Section (2.1.1), since this choice guarantees the existence of an explicit functional (3.3) being minimized, which allows for using tools from non-convex optimization theory to derive the well-posedness of f_θ as we do in the following Section. Furthermore, parameterizing directly $r_\theta : \mathbb{R}^n \rightarrow \mathbb{R}^n$, instead of considering ∇R_θ in (DEQ-MD), would require to find contractive-type bounds making use of the norm of $f_\theta(\cdot; y)$, which presents further challenges than in the Gaussian case due to the presence of h .

4 Convergence theory

In this section, we prove the well-posedness of the DEQ-MD operator $f_\theta(\cdot; y)$ defined in (DEQ-MD) in the sense of Definition 2.1. To this end, we introduce a non-trivial generalization of [11, Theorem 2], which, to the best of our knowledge, has not been explicitly addressed in the existing literature. Having in mind the structure of the functional Ψ in (3.3) to be minimized, we first study conditions upon which the MD sequence converges to some point x^∞ , then we prove that $x^\infty \in \text{Fix}(f_\theta(\cdot; y))$.

Standard convergence results for first-order optimization schemes rely on the Lipschitz continuity of the gradient of the smooth part ($\text{KL}(y, A\cdot) + R_\theta$ in our case). This condition is not met in our framework, due to the presence of $\text{KL}(y, A\cdot)$. We thus consider a more general smoothness condition for KL expressed in terms of the Bregman potential h , which was first considered in [6] in the convex setting and then extended in [15] to the non-convex case to prove convergence of BPG:

Definition 4.1 (NoLip, L -SMAD, Relative smoothness [6],[15],[38]). *Let $f : \mathbb{R}^n \rightarrow \mathbb{R} \cup \{+\infty\}$ be proper, lower semicontinuous with $\text{dom}(f) \supset \text{dom}(h)$ and differentiable on $\text{int}(\text{dom}(h))$. We say that f satisfies the (NoLip) condition with constant $L > 0$, if the following holds:*

$$\text{There exists } L > 0 \text{ such that } Lh - f \text{ is convex on } \text{int}(\text{dom}(h)) \quad (\text{NoLip})$$

Such condition generalizes the standard notion of L -smoothness to the geometry induced by h . Note indeed that if $h = \frac{1}{2}\|\cdot\|_2^2$ then (NoLip) is equivalent to the standard L -smoothness assumption. We have indeed that the following equivalence holds true [50]:

$$\frac{L}{2}\|x\|_2^2 - f \text{ is convex on } \mathbb{R}^n \iff \|\nabla f(x) - \nabla f(y)\|_2 \leq L\|x - y\|_2 \quad \forall x, y \in \mathbb{R}^n.$$

We now recall for convenience [6, Lemma 7]. It provides the existence of such constant L for the pair $(\text{KL}(y, A\cdot), h)$, justifying the choice of the specific Bregman potential considered.

²For a general h , we have that $\text{Prox}_{\iota_C}^h = \Pi_C^h$, the generalized Bregman projection. In the particular case of h being Burg's entropy, it can be proved that the Bregman projection on the cube coincides with the Euclidean projection (see Appendix A.6).

Lemma 4.2 ([6] Lemma 7). *Let $f : x \mapsto KL(y, Ax)$ and h be the Burg’s entropy, defined in (3.2). Then, for any L satisfying $L \geq \|y\|_1 = \sum_{i=1}^m |y_i|$, the function $Lh - f$ is convex on $\mathbb{R}_{>0}^n = \text{int}(\text{dom}(h))$, i.e. (NoLip) holds.*

By Lemma 4.2, to establish the relative smoothness condition (NoLip) for the full objective $KL(y, A \cdot) + R_\theta$, it thus suffices to verify condition (NoLip) for the regularization term R_θ . Specifically, if (NoLip) holds for the pair (R_θ, h) with constant L' , then it holds for $(KL(y, A \cdot) + R_\theta, h)$ with any $L \geq L' + \|y\|_1$, since the sum of convex functions is still convex (see Appendix B.3.3 for details).

As noted by Hurault et al. [29], verifying condition (NoLip) on the entire interior of $\text{dom}(h)$, which is unbounded, can be challenging. However, this becomes significantly easier when restricting the analysis to a compact subset. The key insight is that the function h becomes strongly convex when restricted to bounded subsets of its domain. If the Hessian $\nabla^2 R_\theta$ is also bounded on such a compact set, one can derive explicit bounds that ensure (NoLip) to hold (see again Appendix B.3.3). For this reason, we include an indicator function in the definition of the objective (3.3), effectively restricting the domain to a compact set. This assumption is not restrictive in practice as normalized image data naturally lie in compact sets such as, e.g., $[0, 1]^n$.

The other key ingredient is the Kurdyka–Łojasiewicz property A.7, a classical and powerful tool used to prove algorithmic convergence in non-convex optimization. Although this property may be difficult to be checked directly, it turns out that is satisfied by a wide class of functions. For instance, subanalytic functions continuous on a closed domain satisfy this property [11]. However, the domain of Ψ (3.3) is in general neither closed nor open (see Appendix B.1). We overcome this difficulty by generalizing [11, Theorem 3.1]. For more details we refer to the Appendix B.1).

4.1 Kurdyka–Łojasiewicz property for subanalytic functions with non-closed domain

In this subsection, we show that property A.7 still holds for subanalytic and coercive functions defined on a non-closed domain. The intuition behind the result is that even when the domain is not closed, if it is possible to separate the critical points of the functional being minimized from the set where the functional is infinite, then A.7 can still be recovered.

Proposition 4.3 (KL with non-closed domain). *Let $\Psi : \mathbb{R}^n \rightarrow \mathbb{R} \cup \{+\infty\}$ be a lower semicontinuous and subanalytic function. If Ψ is coercive, $\Psi|_{\text{dom } \Psi}$ is continuous and such that*

$$S := \{x \in \overline{\text{dom}(\Psi)} \mid \Psi(x) = +\infty\}$$

is closed, then Ψ satisfies the Kurdyka–Łojasiewicz property A.7 at any $x^ \in \text{crit}(\Psi)$.*

Proof. The proof is available in Appendix B.1. □

Thanks to Proposition 4.3, we can then state a key result for the regularized Kullback-Leibler functional with regularization.

Corollary 4.4. *Given $\Psi(\cdot) := KL(y, A \cdot) + \iota_{[0, a]^n} + R_\theta$, if $R_\theta : \mathbb{R}^n \rightarrow \mathbb{R}$ is analytic, then Ψ satisfies the Kurdyka–Łojasiewicz property (A.7).*

Proof. The proof is available in Appendix B.2. □

4.2 Convergence results of DEQ-MD

Thanks to the technical results reported in the previous subsection, we are now ready to state our main theoretical result on the convergence of DEQ-MD.

Proposition 4.5 (Convergence of DEQ-MD with learnable regularization).

Let $R_\theta : \mathbb{R}^n \rightarrow \mathbb{R}$ be an analytic neural network parameterized by parameters $\theta \in \Theta$ and let h be defined as in (3.2). Let $L > 0$ be a constant satisfying (NoLip) for the pair $(KL(y, A\cdot) + R_\theta, h)$, let $a > 0$, and let $x^0 \in \text{int}(\text{dom}(h))$. Then, for every $\tau \in (0, \frac{1}{L})$, the sequence given by:

$$x^{k+1} \in \underset{x \in \mathbb{R}^n}{\text{argmin}} \ \iota_{[0,a]^n}(x) + \langle x - x^k, \nabla (KL(y, A\cdot) + R_\theta(\cdot))(x^k) \rangle + \frac{1}{\tau} D_h(x, x^k) \quad (4.1)$$

converges to $x^\infty(\theta; y, x^0)$, a critical point of the functional Ψ defined in (3.3). In addition, (4.1) can be expressed in closed-form as:

$$\begin{aligned} x^{k+1} &= \Pi_{[0,a]^n} \left(\nabla h^*(\nabla h(x^k) - \tau(\nabla KL(y, Ax^k) + \nabla R_\theta(x^k))) \right) \\ &= \Pi_{[0,a]^n} \left(\frac{x^k}{1 + \tau x^k (\nabla KL(y, Ax^k) + \nabla R_\theta(x^k))} \right). \end{aligned} \quad (4.2)$$

Proof. The proof is available in Appendix B.3. □

Note that the operator in (4.2) corresponds to the MD operator $f_\theta(\cdot; y)$ defined in (DEQ-MD).

Remark 4.6 (Analyticity is not restrictive). *Although analyticity might appear to be a strong assumption, it is often satisfied in practice. Neural networks typically require differentiable activation functions to enable gradient-based training, and many commonly used smooth activations (e.g., SoftPlus, tanh, sigmoid) are analytic. As a result, the entire network – hence the learnable regularizer R_θ – often inherits analyticity as a natural consequence of architectural choices (see Appendix B.2, paragraph 1).*

Remark 4.7 (On the choice of h). *The choice of h as the Burg’s entropy is a standard choice in the literature [6]. The rationale behind this choice lies on the compatibility between the domain of h and the one of $KL(y, A\cdot)$, that is $\text{dom}(h) \subset \text{dom}(KL(y, A\cdot))$. Moreover, upon this choice, it is possible to find an explicit constant $L > 0$ satisfying (4.1) (Lemma 4.2). However, certainly this is not the only possible choice guaranteeing the conclusion of Proposition 4.5 as the two main properties required to h are the compatibility condition as well as the strong convexity of h on bounded sets.*

We conclude this section proving the well-posedness of the DEQ-MD $f_\theta(\cdot; y)$ in (DEQ-MD).

Proposition 4.8 (Well-posedness of DEQ-MD). *Under the same assumptions of Proposition 4.5, the DEQ-MD model (DEQ-MD) is well-posed in the sense of Definition 2.1.*

Proof. By Proposition 4.5, for all $x^0 \in \text{int}(\text{dom}(h))$, the sequence $\{x^k\}_{k \in \mathbb{N}}$ converges to $x^\infty \in \text{crit}(\Psi) \subset \text{dom}(\Psi)$. Recalling the explicit expression for $f_\theta(\cdot; y)$ in (4.2), and observing that $x^k \in \text{int}(\text{dom}(KL(y, A\cdot)))$, we get that:

$$x^\infty = \lim_{k \rightarrow \infty} x^{k+1} = \lim_{k \rightarrow \infty} f_\theta(x^k; y) = f_\theta(\lim_{k \rightarrow \infty} x^k; y) = f_\theta(x^\infty; y).$$

□

5 DEQ-MD implementation

Training a DEQ poses both several theoretical and practical challenges: first a grounded approach for computing fixed points is required; moreover, computing gradients through infinitely many applications of f_θ is memory-intensive, making standard backpropagation infeasible. More precisely, we focus in this Section on these two crucial steps:

- **Forward pass:** it refers to how a fixed point $x^\infty(\theta; y, x^0)$ of $f_\theta(\cdot; y)$, given an initial point x^0 , is computed.
- **Backward pass:** it refers to the computation of the gradients of $L(\theta)$ (2.1) with respect to its weights θ .

5.1 Forward pass

Having defined the DEQ-MD operator $f_\theta(\cdot; y)$ as in (DEQ-MD), we need an effective way to compute a fixed point $x^\infty(\theta; y, x^0)$ given an image y and weights θ .

The fixed points of $f_\theta(\cdot; y)$ are in general not unique since they are critical points of a non convex function. On the other hand, Proposition 4.5 states that convergence holds for any choice of $x^0 \in \text{int}(\text{dom}(h))$. Thus, for any such x^0 , the solution map $\theta \mapsto x^\infty(\theta; y, x^0)$ is single-valued.

Another key aspect is the choice of the step-size $\tau > 0$ guaranteeing convergence. From Proposition 4.5, convergence holds for $\tau \in (0, \frac{1}{L})$, with $L \geq \|y\|_1 + L'$ chosen to satisfy (NoLip) for the pair $(\text{KL}(y, A \cdot) + R_\theta, h)$ and where L' is the NoLip constant for (R_θ, h) . Such L' exists (see Appendix B.3.3), but its computation might be challenging as it requires the computation of the maximum eigenvalue of the Hessian $\nabla^2 R_\theta$, which may be hard to compute. During training, the update of the weights θ would lead indeed to a different instance of R_θ , leading to the need of computing the maximum eigenvalue of $\nabla^2 R_\theta$ each time the weights θ change. Furthermore, for images of standard size (in Section 7 we used 256×256) $\|y\|_1$ is big enough to make τ very small. One may argue that with a normalization of the data this may be avoided, but this would lead in fact to smaller magnitude of the gradients involved in (DEQ-MD), which would balance a smaller $\|y\|_1$. As a consequence, we decided to perform the forward pass not computing such L explicitly, but, rather, by estimating a suitable step-size by means of a backtracking strategy, similarly as done in [29] for PnP approaches. Recalling the definition of Ψ in (3.3), we describe such strategy in Algorithm 1.

Algorithm 1: Backtracking for DEQ-MD

- Input:** Initial $\tau_0 > 0$, parameters $\gamma \in (0, 1)$, $\eta \in (0, 1)$
- 1 **Define:** $T_\tau(x) := \Pi_{[0, a]^n}(\nabla h^*(\nabla h(x) - \tau(\nabla \text{KL}(y, Ax) + \nabla R_\theta(x))))$
 - 2 **Initialize:** $\tau = \tau_0$ and $x^0 \in \text{int}(\text{dom}(h))$
 - 3 **while** $\Psi(x^k) - \Psi(T_\tau(x^k)) < \frac{\gamma}{\tau} D_h(T_\tau(x^k), x^k)$ **do**
 - 4 $\tau \leftarrow \eta \tau$
 - 5 **Update:** $x^{k+1} \leftarrow T_\tau(x^k)$
-

The convergence result stated in Proposition Proposition 4.5 still holds upon this choice:

Corollary 5.1. *The Backtracking procedure described in Algorithm (1) terminates in a finite number of steps and provides a sequence of strictly positive step-sizes $\{\tau_k\}_{k \in \mathbb{N}}$. In addition, the conclusion of Proposition 4.5 still holds under the choice τ_k in (4.1).*

Proof. Proof in Appendix D.2 of [29]. □

Remark 5.2. *In contrast to the case of standard DEQs employed in Gaussian cases (see, e.g., [26]), we preferred a Backtracking strategy over standard acceleration strategies for fixed-point iterations, such as Anderson acceleration [59]. To employ Anderson acceleration, we need to take $\tau \in (0, \frac{1}{L})$ and usually this theoretical step-size is much smaller than the ones given by Backtracking (see Figure 4a). As a consequence, employing backtracking typically leads to faster convergence and, in addition, cheaper computations. Note, moreover, Anderson acceleration is typically applied to accelerate fixed-point iterations exhibiting linear convergence (e.g., contractive mappings), while the iterations (4.2) do not correspond to a fixed point iteration of a contraction map.*

5.2 Backward pass

Given the structure of $f_\theta(\cdot; y)$ in (DEQ-MD), the minimization problem (2.1) needs to be solved to compute optimal weights $\hat{\theta}$. This problem is usually addressed by means of first-order optimization algorithms (e.g., ADAM [32]), hence a tractable way to compute gradients of the loss functional $\mathcal{L}(\cdot)$ needs to be found. We provide in the following a formal computation of such gradients. For $\bar{\theta} \in \Theta$ we want to compute:

$$\nabla_{\bar{\theta}} \mathcal{L}(\bar{\theta}) = \sum_{i=1}^n \nabla_{\bar{\theta}} \ell(x^\infty(\bar{\theta}; y_i, x_i^0), x_i^*). \quad (5.1)$$

Omitting the dependence on $i = 1, \dots, n$ in (5.1), by the chain rule we get:

$$\nabla_{\bar{\theta}} \ell(x^\infty(\bar{\theta}; y, x^0), x^*) = \frac{\partial x^\infty(\bar{\theta}; y, x^0)}{\partial \bar{\theta}}^\top \frac{\partial \ell(x^\infty(\bar{\theta}; y, x^0))}{\partial x}, \quad (5.2)$$

where by $\frac{\partial \cdot}{\partial \bar{\theta}}$ we denote the formal Jacobian matrix of the function $\theta \mapsto x^\infty(\theta; y, x^0)$ w.r.t. θ and $\frac{\partial \cdot}{\partial x}$ is the derivative of ℓ w.r.t.. its argument. We refer to Remark 5.3 for more details on how to make such derivation precise in a non-smooth setting.

In (5.2), the quantity $\frac{\partial x^\infty(\bar{\theta}; y, x^0)}{\partial \bar{\theta}}$ is difficult to deal with as it is the output of the infinitely many iterations of the mapping $f_\theta(\cdot; y)$. To make such computation possible, for a fixed $\bar{\theta} \in \Theta$, the quantity $x^\infty(\bar{\theta}; y, x^0)$ can be computed by exploiting the fixed point equation $x^\infty(\bar{\theta}; y, x^0) = f_{\bar{\theta}}(x^\infty(\bar{\theta}; y, x^0); y)$. We detail this in the following, using the shorthand notation $x^\infty(\bar{\theta})$ to indicate $x^\infty(\bar{\theta}; y, x^0)$ and $f_{\bar{\theta}}(\cdot)$ to indicate $f_{\bar{\theta}}(\cdot; y)$. To avoid ambiguities, we will make precise the points where the functions are evaluated explicitly. For all $\theta \in \Theta$, we define the function $F : \Theta \rightarrow \mathbb{R}^n$ by

$$F(\theta) := x^\infty(\theta) - f_\theta(x^\infty(\theta)),$$

which is identically equal to zero by Proposition 4.8. We can thus write:

$$\frac{dF}{d\theta} = \frac{\partial x^\infty}{\partial \theta} - \frac{df_\theta(x^\infty)}{d\theta} = 0, \quad (5.3)$$

where $d \cdot / d\theta$ denotes the total derivative w.r.t.. θ . We get:

$$\left. \frac{df_\theta(x^\infty(\theta; y, x^0))}{d\theta} \right|_{\theta=\bar{\theta}} = \left. \frac{\partial f_{\bar{\theta}}(x)}{\partial x} \right|_{x=x^\infty} \frac{\partial x^\infty(\theta; y, x^0)}{\partial \theta} \Big|_{\theta=\bar{\theta}} + \left. \frac{\partial f_\theta(x^\infty(\bar{\theta}; y, x^0))}{\partial \theta} \right|_{\theta=\bar{\theta}}. \quad (5.4)$$

From (5.4) and (5.3), it is thus possible to get the general linear equation solved by the Jacobian of the function $\theta \mapsto x^\infty(\theta)$, which reads:

$$\left(I - \left. \frac{\partial f_{\bar{\theta}}(x)}{\partial x} \right|_{x=x^\infty} \right) \frac{\partial x^\infty(\bar{\theta}; y, x^0)}{\partial \theta} = \left. \frac{\partial f_{\bar{\theta}}(x^\infty(\bar{\theta}; y, x^0))}{\partial \theta} \right|. \quad (5.5)$$

Denoting now by $\|\cdot\|$ the spectral norm, if $\left\| \left. \frac{\partial f_{\bar{\theta}}(x^\infty)}{\partial x} \right| \right\| < 1$, then $\left(I - \left. \frac{\partial f_{\bar{\theta}}(x^\infty)}{\partial x} \right| \right)$ is invertible and there exists a unique solution to (5.5) given by:

$$\frac{\partial x^\infty(\bar{\theta}; y, x^0)}{\partial \theta} = \left(I - \left. \frac{\partial f_{\bar{\theta}}(x)}{\partial x} \right|_{x=x^\infty} \right)^{-1} \left. \frac{\partial f_{\bar{\theta}}(x^\infty(\bar{\theta}; y, x^0))}{\partial \theta} \right|, \quad \forall \bar{\theta} \in \Theta, \quad (5.6)$$

which can be plugged in (5.2) to get the desired expression.

In several contexts, inverting the matrix arising in (5.6) can be computationally expensive or even infeasible, as is often the case with implicit neural networks. In the following section, we present an approximation strategy that circumvents this limitation and enables efficient computation.

Remark 5.3 (Implicit differentiation in the non-smooth setting). *Note that due to the presence of the non-smooth projection operator $\Pi_{[0,a]^n}$ in the DEQ-MD layer (DEQ-MD), the previous computations relying on (5.2) are only formal. The appropriate framework to compute derivatives and chain rules in the non-smooth case is the one of conservative derivatives (see, e.g., [12, 13]), which we did not consider in our work given the more practical focus on the use of DEQ-MD in the context of image reconstruction.*

5.2.1 Jacobian-Free Backpropagation

In recent years, research on implicit networks has led to the use of a technique called Jacobian-Free Backpropagation (JFB) [25] where the inverse of the Jacobian matrix appearing in (5.6) is replaced by the identity matrix. A possible interpretation of JFB is a zeroth-order approximation to the Neumann series of $\frac{\partial f_\theta(x^\infty)}{\partial x}$ since there holds:

$$\left(I - \frac{\partial f_\theta(x^\infty)}{\partial x} \right)^{-1} = \sum_{k=0}^{+\infty} \left(\frac{\partial f_\theta(x^\infty)}{\partial x} \right)^k,$$

which holds whenever $\left\| \frac{\partial f_\theta(x^\infty)}{\partial x} \right\| < 1$. Although this approximation may seem overly simplistic, it has been shown to work effectively in many practical situations. Specifically it was shown in [25] that, upon suitable assumptions, while the gradients computed using this technique differ from the theoretical gradients, they point towards actual descent directions for the functional $L(\cdot)$, thus allowing its decrease and enabling successful training. In [14], estimates in operator norm of the difference between the true Jacobian and the JFB-Jacobian are given. Using this approach simplifies the calculation of the gradients of $L(\cdot)$ to:

$$\nabla_{\bar{\theta}} \mathcal{L}(\bar{\theta}) \approx \sum_{i=1}^n \frac{\partial f_{\bar{\theta}}(x^\infty(\bar{\theta}; y_i, x_i^0); y_i)^T}{\partial \theta} \frac{\partial \ell(x^\infty(\bar{\theta}; y_i, x_i^0), x_i^*)}{\partial x}, \quad \bar{\theta} \in \Theta. \quad (5.7)$$

In the case of f_θ defined (DEQ-MD), we remark that there is no theoretical guarantee that $\left\| \frac{\partial f_\theta(x^\infty)}{\partial x} \right\| < 1$ due the lack of convexity of the functional Ψ . However, we found out numerically that the relation holds with a non-strict (that is, with \leq) inequality. Notice that the expression in (5.7) can be computed formally in this case, although there is no theoretical guarantee about the effectiveness of the approximation in this case. Nevertheless, as shown in the next Section 6, this approach still works well in practice.

Remark 5.4 (DEQs in practice). *It is useful to remind here that the infinite depth aspect of a DEQ is primarily a theoretical concept. In practice, a finite number of iterations $N > 0$ in the forward pass is computed to obtain a sufficiently accurate approximation of a fixed point within a certain tolerance. Hence, in practice, x^∞ shall be thought of as the output of an N -layered network with N sufficiently large. This might suggest that standard backpropagation could be used to calculate the gradients of interest in (5.2). Note, however, that even with a small N , memory issues quickly arise, since f_θ can be arbitrarily wide. This highlights one of the advantages of the gradient calculation method presented above: regardless of the number of iterations required in the forward pass, the gradients are indeed computed with constant memory [5], meaning it is only necessary to differentiate $f_\theta(\cdot; y)$ at the fixed point as shown in (5.7).*

6 Numerical implementation

In this section, we discuss the details concerned with the image datasets, the network architecture and the implementation of the proposed DEQ-MD model. In particular, we discuss the parameterization of the deep regularization function, for which we propose two different possibilities, and their corresponding architectures. Following this, we detail both the

forward-pass and some computational details of the proposed training methodology. For reproducibility purposes, the code used for the following experiments is available at <https://github.com/christiandaniele/DEQ-MD>.

6.1 Image and training details

In this section we present the image dataset considered, the data generation procedure and the training details. For image assessment, we will use the following three standard image quality metrics: PSNR, SSIM and LPIPS (see Appendix C.)

6.1.1 Image Dataset

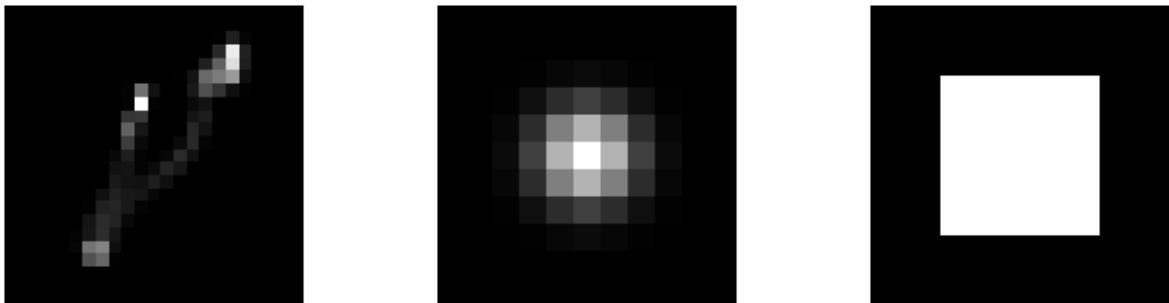
For all experiments, we used the Berkeley image Segmentation Dataset 500 (BSDS500), a dataset of 500 natural RGB images resized to 256x256 by cropping a window of the desired size at the center of the original image. We used 406 images for training, 48 for validation and 46 for test. The dataset is available at <https://www.kaggle.com/datasets/balraj98/berkeley-segmentation-dataset-500-bsds500>.

6.1.2 Data Generation

We generate data using the model

$$y = \text{Pois}(\alpha Ax),$$

where $A \in \mathbb{R}_+^{n \times n}$ is a convolution operator and $\alpha > 0$ allows to modulate the intensity of Poisson noise. In Figure 1 we present a selection of kernels associated with the operator A available within the DeepInverse library³. We considered three levels of noise $\alpha \in \{100, 60, 40\}$ corresponding to low, medium and high amount of Poisson noise and trained a DEQ-MD model for each level of noise and each kernel.



(a) Motion blur kernel

(b) Gaussian Kernel

(c) Uniform kernel

Figure 1: The 3 blur kernels used in the experiments. (a) is a real-world camera shake kernel, see [35]. (b) is a 11×11 Gaussian kernel with standard deviations $\sigma = 1.2$. (c) is a 9×9 uniform kernel.

6.1.3 Training loss and optimizers

As a training loss we used the supervised MSE loss:

$$\ell(x^*, x^\infty) = \|x^* - x^\infty\|_2^2, \quad (6.1)$$

see 6.4 for more details. As optimizer, we considered ADAM [32] initialized with random weights and with piecewise constant step-size $\gamma = 5 \times 10^{-4}$, that is halved after 25 iterations.

³<https://deepinv.github.io/deepinv/>

The JFB strategy (section 5.2.1) was employed to approximate stochastic gradients. Training was performed over 50 epochs and optimal weights were chosen so as to maximize the PSNR on the validation set.

6.2 Deep regularization: parameterization

We consider the following two parameterizations of the regularization function $R_\theta : \mathbb{R}^n \rightarrow \mathbb{R}$ in (DEQ-MD):

- **Scalar Neural network (DEQ-S)** where R_θ is a neural network which maps an image input into a scalar value, e.g. a convolutional neural network (Figure 2a);
- **RED regularization (DEQ-RED)** where R_θ follows a Regularization by Denoising (RED) parameterization, firstly proposed in [47, Section 5.2] and subsequently employed, e.g., in [30] in the form $R_\theta(x) = \frac{1}{2}\|x - N_\theta(x)\|_2^2$, with $N_\theta : \mathbb{R}^n \rightarrow \mathbb{R}^n$. The network N_θ can be chosen, for instance, as a Denoising CNN (DnCNN) [61], see Figure 2b for an illustration of the architecture. Note that contrary to plug-and-play approaches, N_θ is trained directly on the task of interest, that is image reconstruction under Poisson noise.

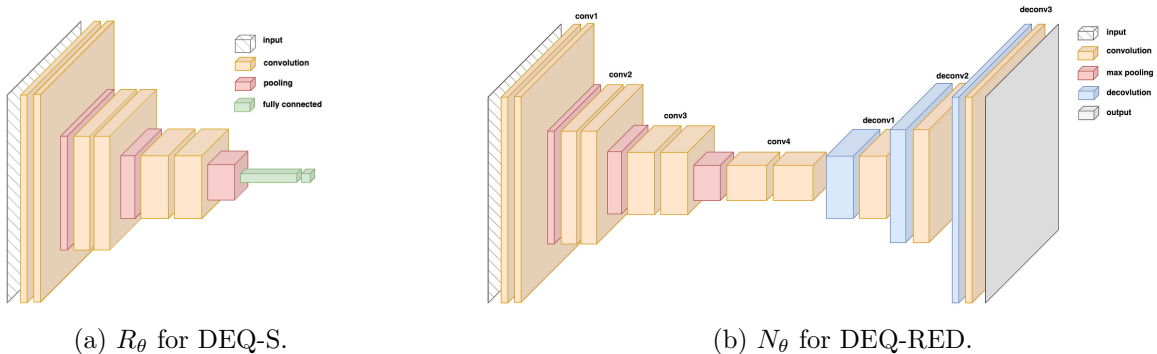


Figure 2: Illustration of the two different networks employed for the parameterization of the regularization function.

Employing the latter strategy allows for pre-training N_θ on, e.g. a denoising task, which generally leads to a better initialization of the network weights. This has the advantage to accelerate convergence during training and, potentially, to achieve better critical points of the loss function (see Appendix D). As observed [49], parameterizing directly R_θ via a scalar neural network may lead to poorer performance.

6.2.1 Network architecture

For the DEQ-S regularization we considered a Convolutional neural network with residual connections as in [23].

For DEQ-RED the choice was the DnCNN architecture introduced in [61]: it is composed of a series of convolutional layers with ReLU activation functions which we replaced by Softplus activations defined by:

$$\text{Softplus}_\beta(x) = \frac{1}{\beta} \log(1 + \exp(\beta x)),$$

which makes the corresponding R_θ differentiable as required. We recall that the greater the parameter $\beta > 0$ is, the more similar the Softplus function becomes to ReLU.

In the following table we report the number of trainable parameters.

Network	CNN (for DEQ-S)	DnCNN (for DEQ-RED)
Activation function	Softplus $_{\beta}$, $\beta = 100$	Softplus $_{\beta}$, $\beta = 100$
Trainable parameters θ	$\approx 5 \times 10^6$	$\approx 3 \times 10^5$

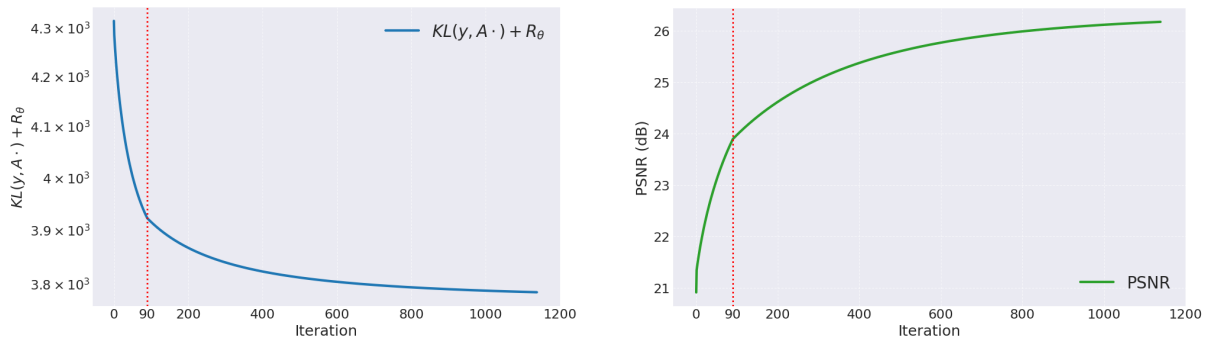
6.3 Forward pass

We discuss here the details of the implementation regarding the forward pass. Recalling the analytic formula of (DEQ-MD), we chose here $a = 1$, which is reasonable for natural images normalized in the range $[0, 1]$. In the spirit of DEQs, we stopped the algorithm when accurate (up to numerical precision) convergence is achieved, that is when the following stopping condition is met:

$$\frac{\|x^{k+1} - x^k\|}{\|x^{k+1}\|} < \epsilon = 2.5 \times 10^{-5}.$$

This value of this tolerance was selected based on empirical observation during numerical experimentation, representing an optimal trade-off: sufficiently small to ensure accuracy, yet large enough to maintain computational efficiency by preventing an excessive number of iterations.

We now report and comment some numerical results obtained at test time by running the forward pass of the proposed DEQ-RED approach on a Gaussian deblurring task with $\alpha = 40$ (see Section 6.1.2 and Figure 1). Figure 3a illustrates the interpretability of the approach: running the DEQ-MD forward pass corresponds to minimize $KL(y, A \cdot) + R_{\theta}(\cdot)$, as detailed in Section 4. On the other hand, Figure 3b shows that PSNR metric is increasing along iterates, with the final iterate maximizing it, which shows the adequacy of the minimization functional to the task considered in terms of reconstruction quality. We stress that this behavior was consistently observed on all the images considered for testing.



(a) Functional values evaluated on the MD sequence.

(b) PSNR improvement along MD iterations.

Figure 3: DEQ-MD forward pass at test time: functional values decrease and PSNR improvement along iterations.

Figure 4a highlights the effectiveness of the backtracking strategy used to estimate admissible step-sizes guaranteeing convergence. Note that the such step-sizes are way bigger than theoretical one, which allows for faster algorithmic convergence. Figure 4b demonstrates the decrease in relative error across iterations. We observe a correlation between changes in the step-size and variations in the relative error, as indicated by the vertical dashed red line.

6.3.1 On the choice of the initialization

Given the non-convex optimization regime where we are considering, the operator $f_{\theta}(\cdot; y)$ (DEQ-MD) may have multiple fixed points associated to the multiple critical points of the functional we are minimizing (Proposition 4.5). The choice of the initialization may thus affect

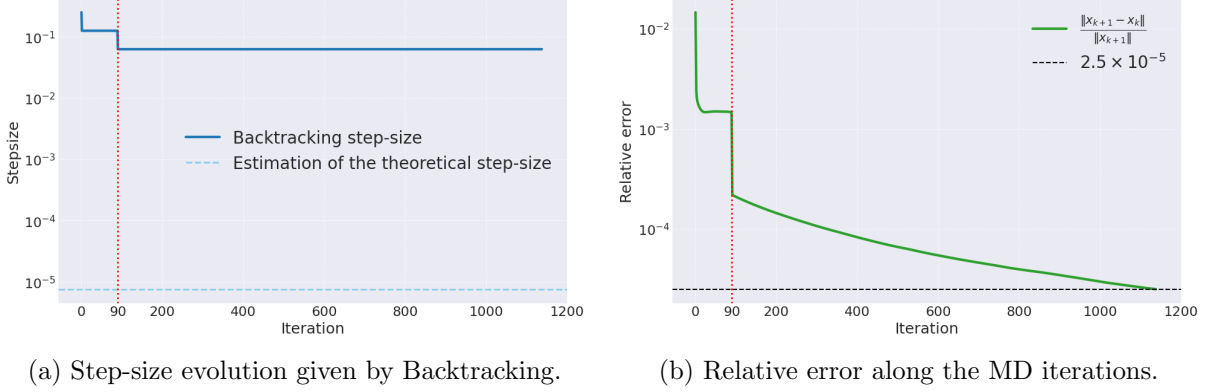


Figure 4: DEQ-MD forward pass at test time: step-size variations due to backtracking and relative error behavior. The estimation of the theoretical step-size is computed as $\bar{\tau} = \frac{1}{L}$, where $L = \|y\|_1$ is the constant satisfying (NoLip) for the pair $(\text{KL}(y, A\cdot), h)$. This value provides an upper bound to the theoretical step-size $\tau < \frac{1}{L+L'} < \frac{1}{L} = \bar{\tau}$, where L' is the constant satisfying (NoLip) for the pair (R_θ, h) .

the point the algorithm converges to, and, as such, it can be considered as an hyper-parameter affecting the quality of the results. Furthermore, in practice, the choice of initialization inputs algorithm efficiency as it impacts the number of iterations needed to get convergence. We thus analyzed four different choices of initializations x^0 in the forward pass:

- **Adjoint-based:** $x^0 = A^*y$.
- **Random:** the components of x^0 are drawn independently from a uniform distribution, that is $x_i^0 \sim \mathcal{U}((0, 1))$ for all $i = 1, \dots, n$.
- **Total Variation reconstruction:** x^0 is chosen as the numerical solution to:

$$x^0 \in \underset{x \geq 0}{\operatorname{argmin}} \text{KL}(y, Ax) + \lambda \text{TV}_\epsilon(x), \quad (6.2)$$

with $\lambda > 0$, where TV_ϵ denotes a smoothed version of the Total Variation (TV) regularization functional. TV regularization is a widely used technique, particularly effective for noise reduction and image reconstruction tasks [48]. It operates by promoting solutions that have sparse gradients, which translates to preserving sharp edges while smoothing out noise in homogeneous regions. This approach is particularly beneficial for images containing piecewise constant or piecewise smooth structures. The TV functional in its natural expression is convex but not differentiable in $x = 0$. For this reason, we smoothed it by adding a small perturbation depending on $\epsilon > 0$, that is by considering:

$$\text{TV}_\epsilon(x) = \sum_{i=1}^{N-1} \sum_{j=1}^{N-1} \sqrt{(x_{i,j+1} - x_{i,j})^2 + (x_{i+1,j} - x_{i,j})^2 + \epsilon},$$

where here $x \in \mathbb{R}^{N \times N}$ with $n = N \times N$. The regularizer TV_ϵ is differentiable on $\mathbb{R}^{N \times N}$. We solved problem (6.2) by running Mirror Descent iterations

$$x^{k+1} = \nabla h^*(\nabla h(x^k) - \tau(\nabla \text{KL}(y, Ax^k)) + \lambda \nabla \text{TV}_\epsilon(x^k)) \quad (6.3)$$

till convergence for a suitable choice of the step-size and for an optimal λ chosen so as to maximize the PSNR w.r.t. the ground truth.

- **Richardson-Lucy** [39, 45]: we consider $x^0 = x_{RL}^K$, that is the K -th iteration of Richardson Lucy (RL) algorithm with $K > 0$. The latter is an EM algorithm designed to minimize the Kullback-Leibler functional (1.2) and particularly used in the context of image deblurring, particularly effective for data corrupted by Poisson noise. The multiplicative iteration of the algorithm reads:

$$x^{k+1} = \frac{x^k}{A^* \mathbf{1}} \left(A^* \frac{y}{Ax^k} \right), \quad (6.4)$$

where $\mathbf{1}$ is a vector of ones, i.e., $\mathbf{1} = (1, \dots, 1) \in \mathbb{R}^m$, and division is intended element-wise. Note that in such iterative regularization setting, the choice of an optimal early stopping K corresponds to the choice of an optimal regularization parameter similarly as for λ above.

We compared the choice of the four initializations above by training four different DEQ-RED models following the modalities specified in Section 6.1.3 and using a subset of the image dataset described in Section 6.1.1, with training set size of 50, a validation set size of 20 and a test set size of 20. We considered an image deblurring problem defined in terms of a Gaussian kernel (see Figure 1) and a level of Poisson noise $\alpha = 100$. As shown in Figure 5, in terms of iterations required to achieve convergence for the forward pass, Adjoint-based, TV and RL are comparable, while the Random initialization always requires many more iterations.

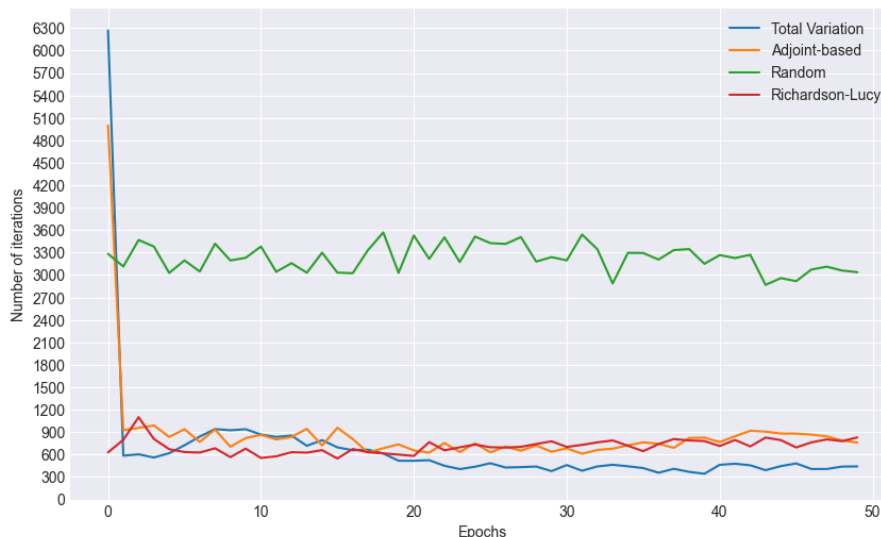


Figure 5: Number of iterations performed in the forward pass to reach the stopping criterion threshold for four different initializations, averaged on the test set, varying with epochs.

In Table 2, we report the computational times needed to get all such initializations and the PSNR values obtained after evaluating each of the four DEQ-MD trained models on the test set. We notice that PSNR values do not change significantly except for x^0 being a random initialization, although we observe that computational time required to get x^0 in the case of TV is way more expensive than the others. As a tradeoff, we thus decided to use for the following tests the Adjoint-based initialization.

We conclude this section by highlighting that we also explored a warm restart initialization technique during the training phase by taking as initialization of the forward pass at epoch $i + 1$ the reconstructions obtained at epoch i . This procedure, which theoretically should accelerate training, did not yield significant effects in terms of either computational time nor reconstruction quality, hence we did not consider it in our numerical results.

	Adjoint-based	TV_ϵ	RL	Random
PSNR (dB)	25.52	25.57	25.54	24.89
CPU time (s)	1e-3	3.05	5e-2	1e-4

Table 2: Average PSNR and CPU times of the solution to the four DEQ-RED models applied on the test set and initialized by choosing the four different initializations considered.

6.4 Training results

Training was performed by following the details described in Section 6.1.3 and using the image dataset in Section 6.1.1. We trained a different DEQ-RED and DEQ-S for each level of noise α and tasks described in Section 6.1.2. As an illustration, we report in Figure 6 the training curves obtained using the DEQ-RED model trained on the Gaussian kernel with $\alpha = 60$. We can notice that after few epochs the metrics stabilize with no significant improvements after 50 epochs at the price of a significant computational overhead. Although theoretical guarantees for JFB are lacking, the empirical results presented in Figure 6 show a positive trend in the validation loss and PSNR. Analogous considerations hold for both DEQ-RED and DEQ-S w.r.t. all level of noise and convolution kernels considered.

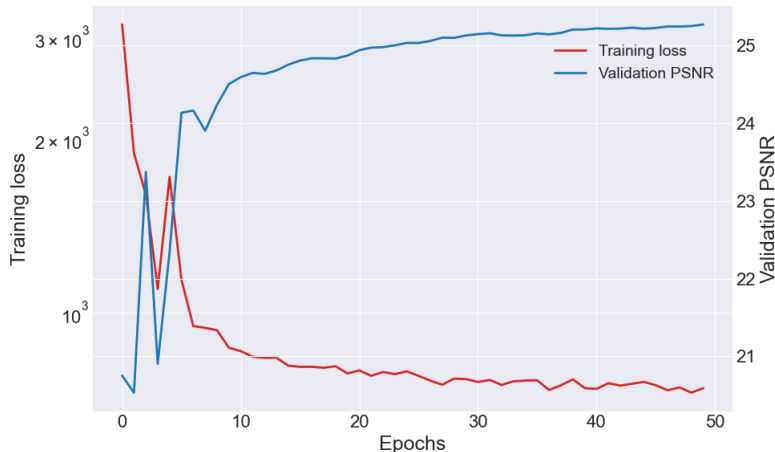


Figure 6: Training curves along epochs for DEQ-RED with $\alpha = 60$ and Gaussian kernel. Training loss evaluated on training set (red), PSNR evaluated on validation set (blue).

To conclude this section, we present a study on the the impact of the choice of loss used for training the DEQ-MD models presented. For this purpose, we compare in the following the MSE loss (6.1) with the choices:

- $\ell(x^*, x^\infty) = \text{KL}(x^*, x^\infty)$;
- $\ell(x^*, x^\infty) = \|x^* - x^\infty\|_1$.

This comparison has been conducted training three DEQ-RED models on the same Gaussian deblurring task using the highest level of noise presented, i.e. $\alpha = 40$ on a test dataset. From Table 3 we can see that all the three metrics provides comparable results with MSE being slightly better. Since, in addition, training KL turned out to be less stable during the training iterations, the MSE loss was employed throughout the experiments.

Table 3: Comparison between different loss functions used in training. Average results computed on the test set with $\alpha = 40$ and Gaussian blur.

Loss Function	PSNR \uparrow	SSIM \uparrow	LPIPS \downarrow
MSE	25.9250	0.7375	0.2921
KL	<u>25.8152</u>	0.7313	0.3198
L1	25.7876	<u>0.7341</u>	<u>0.3144</u>

7 Numerical experiments

In this section, we present several numerical experiments validating the DEQ-MD framework. We tested our method under the settings described in Section 6.1.2. The image reconstructions obtained are compared with the following model-based and data-driven approaches tailored to Poisson noise removal:

– **Model-based:**

- **Richardson Lucy (RL)** [39, 45] algorithm (6.4): we ran the algorithm for a fixed maximum number of 100 iterations and chose as optimal early stopping the one whose corresponding iterate maximizes the PSNR w.r.t. ground truth.
- **KL+smoothed Total Variation (KL+TV)** (6.2): we ran the instance (6.3) of MD for different values of λ , choosing as optimal value the one for which the corresponding solution maximizes the PSNR w.r.t. ground truth.

- **Data-driven:** PnP-based methods tailored for Poisson Inverse Problems in the form (1.1) were considered in [29] and addressed using MD as an underlying optimization algorithm. In this framework, the denoiser considered takes the form of a generalization of a gradient step denoiser, and it is trained on data corrupted by Inverse Gamma noise. By choosing h as the Burg’s entropy (3.2), the Bregman proximal operator associated turns out to be the MAP estimator of an Inverse Gamma image denoising problem. To be more precise, considering a potential $g_\gamma : \mathbb{R}^n \rightarrow \mathbb{R}$ defined by:

$$g_\gamma(x) = \frac{1}{2} \|x - N_\gamma(x)\|_2^2,$$

the corresponding Bregman denoiser takes the form:

$$\mathcal{B}_\gamma(x) = x - (\nabla^2 h(x))^{-1} \nabla g_\gamma(x).$$

Such denoiser is then trained on different levels γ of Inverse Gamma noise.

Within this framework, two different algorithms can be considered:

- **B-RED:**

$$x^{k+1} = \Pi_{[0,1]^n} (\nabla h^*(\nabla h(x^k)) - \tau(\lambda \nabla \text{KL}(y, Ax^k) + \nabla g_\gamma(x^k))).$$

Here, the step-size $\tau > 0$ is chosen by employing the backtracking strategy in Algorithm 1, $\lambda > 0$ is the regularization parameter and γ is the level of Inverse Gamma noise to be tuned.

- **B-PnP:**

$$x^{k+1} = \mathcal{B}_\gamma(\nabla h^*(\nabla h(x^k)) - \tau \nabla \text{KL}(y, Ax^k)),$$

where the step-size is chosen such that $\tau L < 1$, with L given by Lemma 4.2.



Figure 7: Reconstruction comparison in terms of PSNR, SSIM and LPIPS for image deblurring with Gaussian blur and Poisson noise with $\alpha = 40$.

In Figure 7, we evaluate the results obtained by the different methods on a Gaussian deblurring task (Fig. 1b) at test time with noise level $\alpha = 40$. Notice that the absence of explicit regularization for Richardson-Lucy (RL) yields poor reconstruction results. In contrast, the reconstruction computed using the KL+TV $_{\epsilon}$ model provides good reconstruction quality, though it remains inferior to both Bregman PnP and DEQ-RED. We observed that DEQ-S struggles to effectively remove image noise. This aligns with findings in [49], where it is observed that directly parameterizing regularization functional through a neural network can lead to suboptimal results. Regarding B-RED and B-PnP, we observe that their performance is remarkably similar, with B-RED performing slightly better in terms of the three metrics. Finally, DEQ-RED provides the best reconstruction, achieving a significantly higher PSNR value.

Figure 8 illustrates a more challenging scenario involving motion blur. The detailed features of the 'Clean' image are hardly discernible in the 'Observed' image due to the action of the blur. The RL method proves particularly ineffective on this particular task, while the KL+TV $_{\epsilon}$ solution introduces excessive smoothing. Both B-RED and B-PnP reconstructions are visually appealing; however, artifacts are noticeable, especially in the background where most details appear lost with a general tendency towards over-smoothing. Note that the DEQ-S reconstruction over-smooths details leaving somewhat noisy the background. DEQ-RED achieves the best overall reconstruction metrics, with texture-preserving smoothing enforced both in the background and in the textured areas. This example highlights the robustness of DEQ methods, and in particular of DEQ-RED, to artifacts. On the other hand, PnP approaches, while providing visually appealing denoised reconstructions tend to significantly over-smooth images.

Table 4 presents a comparative analysis of the methods on a test set composed by 46 images, aggregating results across three noise levels and three kernels. For the low and medium noise scenario ($\alpha \in \{100, 60\}$), DEQ-RED consistently achieved the highest values across all three metrics. At $\alpha = 60$, B-RED edged out DEQ-RED slightly in terms of PSNR and SSIM, though their overall metric values remained very close. In the high noise case ($\alpha = 40$), B-RED delivered

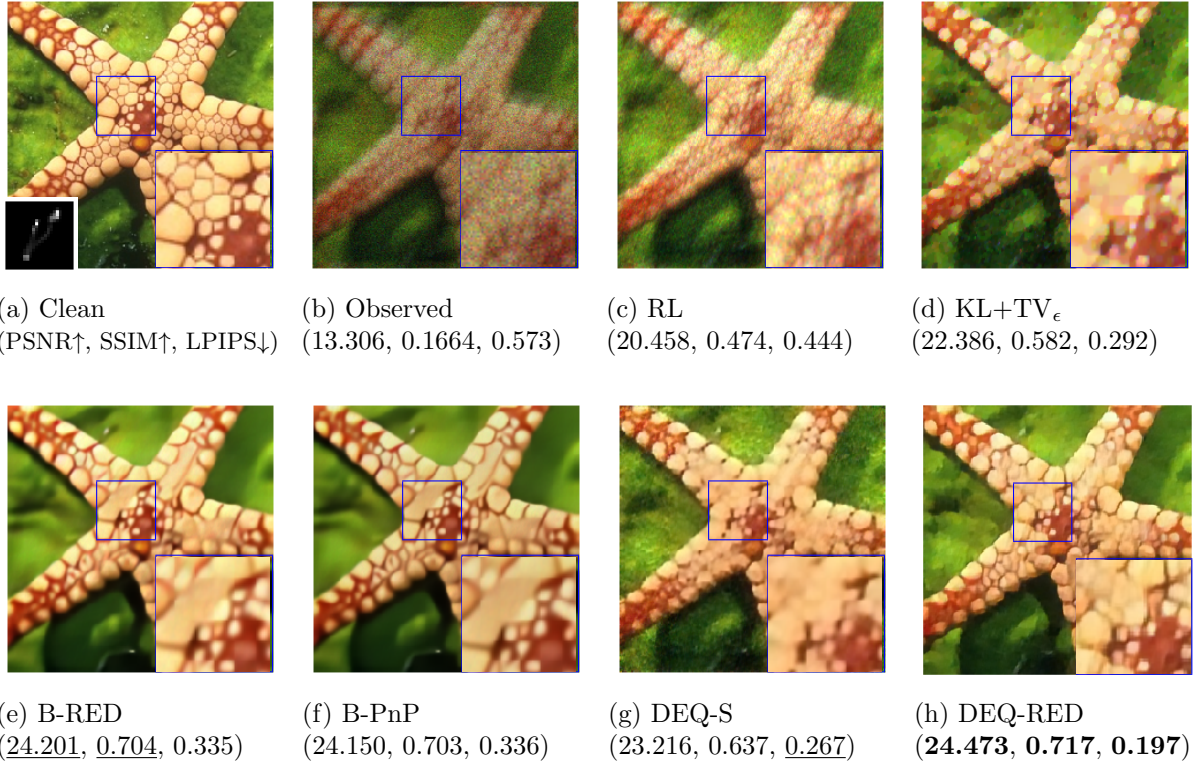


Figure 8: Reconstruction comparison in terms of PSNR, SSIM and LPIPS for image deblurring task with motion blur and Poisson noise with $\alpha = 60$.

Table 4: Performance comparison of different methods under levels of Poisson noise ranging from low to high $\alpha \in \{100, 60, 40\}$ averaged on the three convolution kernels considered. Evaluations are made on the test set.

Method	$\alpha = 100$			$\alpha = 60$			$\alpha = 40$		
	PSNR \uparrow	SSIM \uparrow	LPIPS \downarrow	PSNR \uparrow	SSIM \uparrow	LPIPS \downarrow	PSNR \uparrow	SSIM \uparrow	LPIPS \downarrow
RL	22.7381	0.5379	0.5570	22.2968	0.5111	0.6017	21.9496	0.4901	0.6373
KL+TV $_{\epsilon}$	23.9879	0.6304	<u>0.3888</u>	23.5203	0.6045	<u>0.4254</u>	23.1438	0.5844	0.4547
B-RED	<u>25.0710</u>	<u>0.6939</u>	0.4120	<u>24.6566</u>	<u>0.6723</u>	0.4384	24.4603	0.6530	<u>0.4533</u>
B-PnP	24.8976	0.6847	0.4417	24.5818	0.6674	0.4401	24.2912	<u>0.6612</u>	0.4534
DEQ-S	24.2080	0.6730	0.3935	23.7252	0.6221	0.4346	23.4423	0.5912	0.4591
DEQ-RED	25.4245	0.7091	0.3058	24.9087	0.6826	0.3354	<u>24.4586</u>	0.6626	0.3571

a slightly superior PSNR. Conversely, DEQ-RED consistently proved to be the best performer for LPIPS and SSIM.

In Table 5 we present the number of hyperparameters required to obtain the reconstructions using all methods considered. RL and KL+TV $_{\epsilon}$ need each one only one parameter to be tuned per image. In contrast, B-RED and B-PnP require the tuning of two pairs of parameters: $(\lambda_{\text{in}}, \gamma_{\text{in}})$ and $(\lambda_{\text{algo}}, \gamma_{\text{algo}})$. This requirement stems from the methodology proposed in [29], where an initial fixed number of iterations is performed using $(\lambda_{\text{in}}, \gamma_{\text{in}})$ as regularization parameter/denoiser hyper-parameter to achieve a robust initialization. Subsequently, the primary algorithm is run using the second set of parameters $(\lambda_{\text{algo}}, \gamma_{\text{algo}})$. Note however, that despite the theoretical need for parameter tuning for each reconstruction, in [29] optimal parameter values depending solely on the noise level α are provided. Contrarily to the previous methods, the proposed algorithms, DEQ-S, DEQ-RED are instead parameter-free, = having been trained for a specific forward operator and noise levels. Note that, however, both DEQ-MD

approaches showed good generalization properties w.r.t. different task and noise level, which will be discussed in Section 7.1.1.

Table 5: Number of hyperparameters needed at inference time for each reconstruction method considered.

Method	Number	Parameters type
RL	1	N^{stop} : Optimal early stopping
KL+TV $_{\epsilon}$	1	λ : Optimal regularization parameter
B-RED	4	$(\lambda_{in}, \gamma_{in}, \lambda_{algo}, \gamma_{algo})$: Initialization/reconstruction parameters
B-PnP	4	$(\lambda_{in}, \gamma_{in}, \lambda_{algo}, \gamma_{algo})$: Initialization/reconstruction parameters
DEQ-S	0	-
DEQ-RED	0	-

We conclude this section presenting in Table 6 the training times, when needed and the CPU times required to conclude a forward pass, i.e. to perform the inference phase and reconstruct the image. The test was executed on the entire test dataset simultaneously, whenever the code implementation supports batch processing.

Table 6: Computational times for the training procedure and inference. The first column reports the total training time for the data-driven approaches. The second column shows the time required to perform inference on the entire test set, while the third column indicates the average time per image on the test set.

Method	Training time (hours)	Time on test set (s)	Average time per image (s)
RL	–	0.55	0.019
KL+TV	–	146.44	3.18
B-RED	216	1900.15	41.30
B-PnP	216	860.11	18.69
DEQ-S	105	1050.34	22.83
DEQ-RED	50	408.94	8.89

The computational times for training the DEQ-MD model were obtained following the modalities described in Section 6.1.3. Values are averaged over the number of noise levels and tasks described in Section 7. For both DEQ-S and DEQ-RED, time per epoch is higher in early epochs and then decreases until it stabilizes. An explanation of this behavior could be that in early epochs a lot of iterations are needed to get convergence in the forward pass (see the Adjoint-based case in Figure 5) while later this effect is mitigated. This could be further improved using a pre-training strategy (see Appendix D). For both B-RED and B-PnP, training times are reported w.r.t. the training of the Bregman Denoiser, whose training modalities can be found in [29].

Regarding inference time, model-based RL stands out as the fastest algorithm, exhibiting a significant speed advantage over other methods. Among the learned approaches, DEQ-RED offers competitive CPU time. This efficiency stems from the use of the backtracking strategy, which is effectively implemented to leverage GPU parallelization and batch processing. Note that, however, such time gain is not observed using the DEQ-S method as the CNN employed requires more computation time within its fully-connected layers.

7.1 Generalization to different tasks/noise levels

In this section we discuss the generalization property of the DEQ-MD approaches presented in two respects:

- Does a DEQ-MD model trained on a level of noise α generalize on a level of noise $\alpha' \neq \alpha$?
- Does a DEQ-MD model trained on a deblurring task using a certain convolution kernel generalize to a different task, such as, e.g. a super resolution problem?

For the following discussion, we focus only on the DEQ-RED method, which shows superior performances w.r.t DEQ-S as extensively discussed before.

7.1.1 Generalization to different noise levels

In order to generalize a DEQ-MD model trained on a noise level α to a different noise level $\alpha' \neq \alpha$ not seen during training, we consider the following λ -penalized instance of the DEQ-MD approach:

$$f_{\theta}^{\lambda}(x; y) = \Pi_{[0, a]^n} \left(\frac{x}{1 + \tau x (\nabla \text{KL}(y, Ax) + \lambda \nabla R_{\theta}(x))} \right), \quad (7.1)$$

which is associated to the following minimization problem:

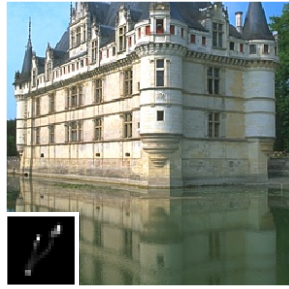
$$\Psi_{\lambda}(x) = \text{KL}(y, Ax) + \lambda R_{\theta}(x) + \iota_{[0, a]^n}(x)$$

for which all convergence guarantees discussed in Section 4.2 hold. The parameter λ plays here the role of an actual regularization parameter whose magnitude should weight more/less the regularization against the KL data term depending on the ration α/α' . A natural choice thus consists in considering as $\lambda = \frac{\alpha}{\alpha'}$. To evaluate the effect of this choice, we tested all considered kernels by evaluating DEQ-MD models trained on a single noise level $\alpha \in 100, 60, 40$ at different test noise levels $\alpha' \neq \alpha$, using the rule above to select λ in (7.1). Results are reported in Table 7.

Table 7: Generalization of DEQ-MD w.r.t. different noise levels.

α training	α inference = 100			α inference = 60			α inference = 40		
	PSNR \uparrow	SSIM \uparrow	LPIPS \downarrow	PSNR \uparrow	SSIM \uparrow	LPIPS \downarrow	PSNR \uparrow	SSIM \uparrow	LPIPS \downarrow
100	<u>25.4245</u>	<u>0.7091</u>	<u>0.3058</u>	24.7776	0.6778	0.3465	24.2627	0.6513	0.3816
60	25.4828	0.7112	0.3020	24.9087	<u>0.6826</u>	<u>0.3354</u>	<u>24.3854</u>	<u>0.6568</u>	<u>0.3689</u>
40	25.4006	0.7079	0.3077	<u>24.8800</u>	0.6841	0.3335	24.4586	0.6626	0.3571

For each noise level, we refer to the metrics value on the diagonal as the reference ones, since in those cases the model has been tested on the same level of noise seen during training. We note that upon the choice of λ discussed above, DEQ-MD appear to be easily generalizable to unseen noise levels, especially when the inference is performed on a lower intensity of Poisson noise w.r.t the one in the training. In particular, for $\alpha = 100$, the best model appears to be the one trained on $\alpha = 60$ with $\alpha = 40$ providing performances close to the reference values. The same consideration holds for the inference with $\alpha = 60$ and the model trained on $\alpha = 40$. While the proposed selection rule for λ might not be the optimal one, it still provides a fairly simple criterion, based only on the knowledge of the noise levels, which streamlines hyperparameter selection. Figure 9 and 10 visually demonstrate the effectiveness of the proposed approach.



(a) Clean
(PSNR \uparrow , SSIM \uparrow , LPIPS \downarrow)



(b) Observed
(14.564, 0.186, 0.514)



(c) $\alpha^{\text{train}} = 100, \lambda = 1$
(23.353, **0.709**, 0.312)



(d) $\alpha^{\text{train}} = 60, \lambda = 0.6$
(23.317, 0.704, 0.313)



(e) $\alpha^{\text{train}} = 40, \lambda = 0.4$
(**23.395**, 0.709, **0.305**)

Figure 9: Generalization study on different levels of noise. Test is performed on a deblurring task with motion blur with $\alpha^{\text{test}} = 100$.



(a) Clean
(PSNR \uparrow , SSIM \uparrow , LPIPS \downarrow)



(b) Observed
(17.586, 0.503, 0.5435)



(c) $\alpha^{\text{train}} = 100, \lambda = 5/3$
(24.514, 0.896, 0.090)



(d) $\alpha^{\text{train}} = 60, \lambda = 1$
(24.793, 0.889, **0.074**)



(e) $\alpha^{\text{train}} = 40, \lambda = 2/3$
(**24.885**, **0.896**, 0.083)

Figure 10: Generalization study on different levels of noise. Test is performed on a deblurring task with Gaussian blur with $\alpha^{\text{test}} = 60$.

7.1.2 Generalization to super-resolution

In this section, we study the generalization ability of DEQ-MD models trained on a specific image deblurring task to a related but distinct task: Super-Resolution under Poisson noise. In this setting, an image $y \in \mathbb{R}^m$ is obtained as a degraded version of an image $x \in \mathbb{R}^n$ with $n = s^2m$, according to:

$$y = \text{Poiss}(\alpha SAx),$$

where $S \in \mathbb{R}^{m \times n}$ is a down-sampling operator, s the scale factor and $A \in \mathbb{R}^{n \times n}$ is a convolution operator associated with the kernels shown in Figure 1. The operator S extracts the top-left pixel from each $s \times s$ block. Figure 11 presents results for the case $s = 2$. Even without task-specific training, DEQ-RED exhibits notable generalization to this Super-Resolution setting.

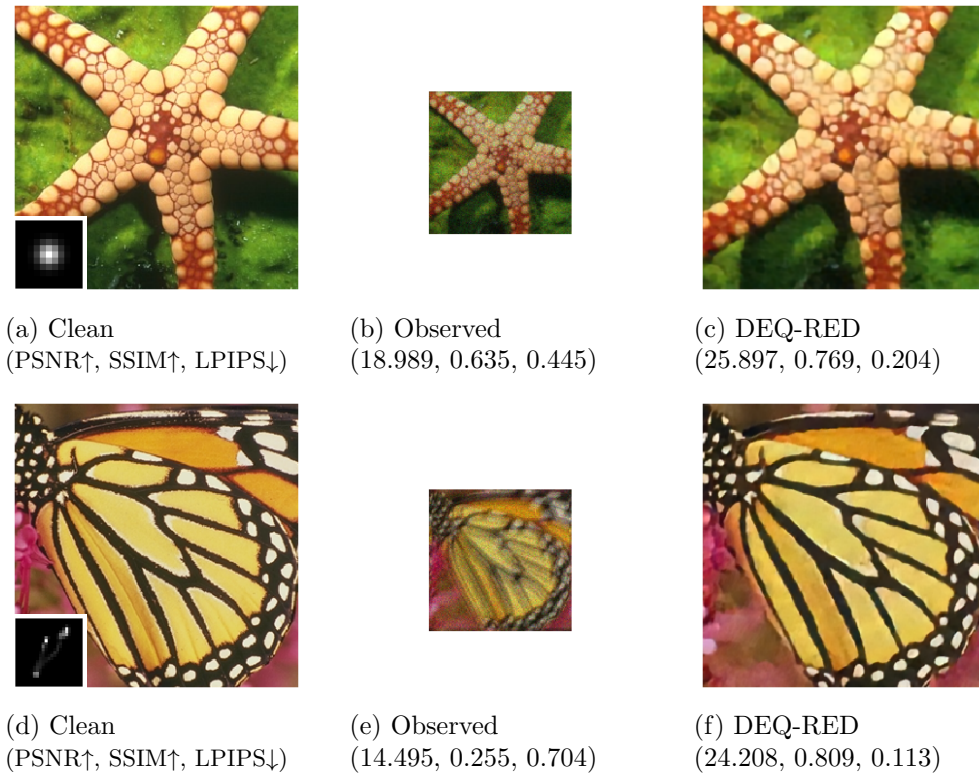


Figure 11: Generalization test to $\times 2$ super-resolution task. First row: Gaussian blur and $\alpha = 60$. Second row: Motion blur and $\alpha = 100$. The value of the metrics for the observed images have been calculated between the clean images and image $(SA)^\top y$.

We observed a degradation of the results for more challenging scale factors $s \geq 3$.

Remark 7.1 (The Importance of normalization). *We stress that in order to get good super-resolution results as the ones in Figure 11, it is important to normalize the forward operator $T = SA$ so as to have $\|T^\top T\|_2 = 1$. In practice, it is numerically important to normalize the operator T , in order to ensure that its overall energy is consistent across different resolutions. This normalization prevents the inversion process from being biased or ill-conditioned due to scale discrepancies introduced by the blur-and-subsample operations. Without such normalization, the reconstructed results tend to be of lower quality, with a noticeable loss of image details and fine structures. The normalization used is available at <https://github.com/christiandaniele/DEQ-MD>.*

8 Conclusions and Outlook

We proposed a novel Deep Equilibrium Model (DEQ) framework, named DEQ-MD, for solving linear Poisson inverse problems, leveraging Mirror Descent as a geometry-aware optimization backbone. Unlike classical Plug-and-Play or unrolled architectures, DEQ-MD learns regularization functionals end-to-end through the fixed point of the MD algorithm with a geometry tailored to the Kullback–Leibler divergence. This approach allows us to bypass standard smoothness and contractivity assumptions typically required in DEQ theory, while still guaranteeing convergence of the reconstruction procedure. Our analysis avoids operator contractivity and instead relies on non-convex optimization principles, enabling greater flexibility in the network design and interpretability through the minimization of an explicit functional. In this context, we established refined convergence results extending [11, Theorem 2] within the Kurdyka–Lojasiewicz framework, providing a broadly applicable tool for handling Kullback–Leibler divergences in the presence of non-convex regularization. Beyond the theoretical framework, our method yields competitive reconstructions using significantly lighter architectures, while offering faster inference and full parameter-free operation at test time. Though developed for the Poisson setting, our formulation is general and potentially applicable to other problems and geometries via suitable choices of the underlying Bregman potential (e.g., phase retrieval [27]).

Looking ahead, we aim to extend convergence guarantees for the Jacobian-Free Backpropagation (JFB) scheme in more general, non-contractive and non-smooth settings, and to integrate self-supervised training strategies. This would further increase the applicability of our approach in domains like microscopy and medical imaging, where ground-truth data is scarce or unavailable.

Acknowledgments

The work of C. Daniele and L. Calatroni was supported by the ANR JCJC project TASKABILE ANR-22-CE48-0010. The work of C. Daniele, L. Calatroni and S. Villa was supported by the funding received from the European Research Council (ERC) Starting project MALIN under the European Union’s Horizon Europe programme (grant agreement No. 101117133).

S. Villa acknowledges the support of the European Commission (grant TraDE-OPT 861137), of the European Research Council (grant SLING 819789), the US Air Force Office of Scientific Research (FA8655-22-1-7034), the Ministry of Education, University and Research (PRIN 202244A7YL project “Gradient Flows and Non-Smooth Geometric Structures with Applications to Optimization and Machine Learning”), and the project PNRR FAIR PE0000013 - SPOKE 10. The research by S. Villa. has been supported by the MIUR Excellence Department Project awarded to Dipartimento di Matematica, Università di Genova, CUP D33C23001110001. S. Villa is a member of the Gruppo Nazionale per l’Analisi Matematica, la Probabilità e le loro Applicazioni (GNAMPA) of the Istituto Nazionale di Alta Matematica (INdAM).

S. Vaiter thanks PEPR PDE-AI (ANR-23-PEIA-0004), the chair 3IA BOGL through the 3IA Cote d’Azur Investments (ANR-23-IACL-0001) and the ANR PRC MAD (ANR-24-CE23-1529). This work represents only the view of the authors. The European Commission and the other organizations are not responsible for any use that may be made of the information it contains.

References

- [1] Jonas Adler and Ozan Öktem. Learned Primal-Dual Reconstruction. *IEEE Transactions on Medical Imaging*, 37(6):1322–1332, 2018.
- [2] Abdullah H. Al-Shabli, Xiaojian Xu, Ivan Selesnick, and Ulugbek S. Kamilov. Bregman

- Plug-and-Play Priors. In *2022 IEEE International Conference on Image Processing (ICIP)*, pages 241–245. IEEE, 2022.
- [3] H. Attouch, J. Bolte, P. Redont, and A. Soubeyran. Proximal Alternating Minimisation and Projection Methods for Nonconvex Problems: An Approach Based on the Kurdyka-Lojasiewicz inequality. *Mathematics of Operations Research*, 35(2):438–457, 2010.
- [4] H. Attouch, J. Bolte, and B. F. Svaiter. Convergence of Descent Methods for Semi-Algebraic and Tame Problems: Proximal Algorithms, Forward–Backward Splitting, and Regularized Gauss–Seidel Methods. *Mathematical Programming*, 137(1-2):91–129, 2013.
- [5] Shaojie Bai, J. Zico Kolter, and Vladlen Koltun. Deep Equilibrium Models. *Advances in Neural Information Processing Systems*, 32, 2019.
- [6] Heinz H. Bauschke, Jérôme Bolte, and Marc Teboulle. A Descent Lemma Beyond Lipschitz gradient continuity: First-order methods revisited and applications. *Mathematics of Operations Research*, 42(2):330–348, 2017.
- [7] Heinz H. Bauschke and Patrick L. Combettes. *Convex Analysis and Monotone Operator Theory in Hilbert Spaces*. CMS Books in Mathematics. Springer, New York, 2011.
- [8] A. Beck. *First-Order Optimisation Methods*. Society for Industrial and Applied Mathematics (SIAM), 2017.
- [9] Mario Bertero, Patrizia Boccacci, Gabriele Desiderà, and Giuseppe Vicidomini. Image Deblurring with Poisson Data: From Cells to Galaxies. *Inverse Problems*, 25(12):123006, 2009.
- [10] E. Bierstone and P. D. Milman. Semianalytic and subanalytic sets. *Publications Mathématiques de l’IHÉS*, 67:5–42, 1988.
- [11] J. Bolte, A. Daniilidis, and A. Lewis. The Lojasiewicz inequality for nonsmooth subanalytic functions with applications to subgradient dynamical systems. *SIAM Journal on Optimization*, 17(4):1205–1223, 2007.
- [12] Jérôme Bolte, Tam Le, Edouard Pauwels, and Tony Silveti-Falls. Nonsmooth implicit differentiation for machine-learning and optimization. In M. Ranzato, A. Beygelzimer, Y. Dauphin, P.S. Liang, and J. Wortman Vaughan, editors, *Advances in Neural Information Processing Systems*, volume 34, pages 13537–13549. Curran Associates, Inc., 2021.
- [13] Jérôme Bolte, Edouard Pauwels, and Samuel Vaiter. Automatic differentiation of nonsmooth iterative algorithms. *Advances in Neural Information Processing Systems*, 35:26404–26417, 2022.
- [14] Jérôme Bolte, Edouard Pauwels, and Samuel Vaiter. One-Step Differentiation of Iterative Algorithms. *Advances in Neural Information Processing Systems*, 36:77089–77103, 2023.
- [15] Jérôme Bolte, Shoham Sabach, Marc Teboulle, and Yakov Vaisbourd. First Order Methods Beyond Convexity and Lipschitz Gradient Continuity with Applications to Quadratic Inverse Problems. *SIAM Journal on Optimization*, 28(3):2131–2151, 2018.
- [16] Silvia Bonettini, Simone Rebegoldi, and Valeria Ruggiero. Inertial Variable Metric Techniques for the Inexact Forward–Backward Algorithm. *SIAM Journal on Scientific Computing*, 40(5):A3180–A3210, 2018.
- [17] Silvia Bonettini, Riccardo Zanella, and Luca Zanni. A Scaled Gradient Projection Method for Constrained Image Deblurring. *Inverse Problems*, 25(1):015002, 2008.

- [18] Charles L. Byrne. Iterative Image Reconstruction Algorithms Based on Cross-Entropy Minimization. *IEEE Transactions on Image Processing*, 2(1):96–103, 1993.
- [19] C.L. Byrne. Accelerating the emml algorithm and related iterative algorithms by rescaled block-iterative methods. *IEEE Transactions on Image Processing*, 7(1):100–109, 1998.
- [20] Antonin Chambolle, Matthias J Ehrhardt, Peter Richtárik, and Carola-Bibiane Schonlieb. Stochastic Primal-Dual Hybrid Gradient Algorithm With Arbitrary Sampling and Imaging Applications. *SIAM Journal on Optimization*, 28(4):2783–2808, 2018.
- [21] Daniela di Serafino, Germana Landi, and Marco Viola. Directional TGV-Based Image Restoration Under Poisson Noise. *Journal of Imaging*, 7(6):99, 2021.
- [22] François-Xavier Dupé, Jalal M. Fadili, and Jean-Luc Starck. A Proximal Iteration for Deconvolving Poisson Noisy Images Using Sparse Representations. *IEEE Transactions on Image Processing*, 18(2):310–321, 2009.
- [23] Zhenghan Fang, Sam Buchanan, and Jeremias Sulam. What’s in a Prior? Learned Proximal Networks for Inverse Problems. *arXiv preprint arXiv:2310.14344*, 2023.
- [24] Mário AT Figueiredo and José M Bioucas-Dias. Restoration of Poissonian Images Using Alternating Direction Optimization. *IEEE Transactions on Image Processing*, 19(12):3133–3145, 2010.
- [25] Samy Wu Fung, Howard Heaton, Qiuwei Li, Daniel McKenzie, Stanley Osher, and Wotao Yin. JFB: Jacobian-Free Backpropagation for Implicit Networks. In *Proceedings of the AAAI Conference on Artificial Intelligence*, volume 36, pages 6648–6656, 2022.
- [26] Davis Gilton, Gregory Ongie, and Rebecca Willett. Deep Equilibrium Architectures for Inverse Problems in Imaging. *IEEE Transactions on Computational Imaging*, 7:1123–1133, 2021.
- [27] Jean-Jacques Godeme, Jalal Fadili, Claude Amra, and Myriam Zerrad. Stable Phase Retrieval With Mirror Descent. *arXiv preprint arXiv:2405.10754*, 2024.
- [28] Zachary T Harmany, Roummel F Marcia, and Rebecca M Willett. This Is SPIRAL-TAP: Sparse Poisson Intensity Reconstruction Algorithms—Theory and Practice. *IEEE Transactions on Image Processing*, 21(3):1084–1096, 2011.
- [29] Samuel Hurault, Ulugbek Kamilov, Arthur Leclaire, and Nicolas Papadakis. Convergent Bregman Plug-and-Play Image Restoration for Poisson Inverse Problems. *Advances in Neural Information Processing Systems*, 36:27251–27280, 2023.
- [30] Samuel Hurault, Arthur Leclaire, and Nicolas Papadakis. Gradient Step Denoiser for Convergent Plug-and-Play. *arXiv preprint arXiv:2110.03220*, 2021.
- [31] Ulugbek S Kamilov, Charles A Bouman, Gregory T Buzzard, and Brendt Wohlberg. Plug-and-Play Methods for Integrating Physical and Learned Models in Computational Imaging: Theory, Algorithms, and Applications. *IEEE Signal Processing Magazine*, 40(1):85–97, 2023.
- [32] Diederik P. Kingma. Adam: A Method for Stochastic Optimization. *arXiv preprint arXiv:1412.6980*, 2014.
- [33] Teresa Klatzer, Savvas Melidonis, Marcelo Pereyra, and Konstantinos C Zygalakis. Efficient Bayesian Computation Using Plug-and-Play Priors for Poisson Inverse Problems. *arXiv preprint arXiv:2503.16222*, 2025.

- [34] Rémi Laumont, Valentin De Bortoli, Andrés Almansa, Julie Delon, Alain Durmus, and Marcelo Pereyra. Bayesian Imaging Using Plug & Play Priors: When Langevin Meets Tweedie. *SIAM Journal on Imaging Sciences*, 15(2):701–737, 2022.
- [35] Anat Levin, Yair Weiss, Fredo Durand, and William T. Freeman. Understanding and Evaluating Blind Deconvolution Algorithms. In *2009 IEEE Conference on Computer Vision and Pattern Recognition*, pages 1964–1971. IEEE, 2009.
- [36] S. Łojasiewicz. Triangulation of Semi-Analytic Sets. *Annali della Scuola Normale Superiore di Pisa, Classe di Scienze*, 18(4):449–474, 1964.
- [37] Stanisław Łojasiewicz. *On Semi-analytic and Subanalytic Geometry*. Instytut Matematyki, Uniwersytet Jagielloński, Kraków, Poland, 1999.
- [38] Haihao Lu, Robert M Freund, and Yurii Nesterov. Relatively Smooth Convex Optimization by First-Order Methods, and Applications. *SIAM Journal on Optimization*, 28(1):333–354, 2018.
- [39] Leon B. Lucy. An Iterative Technique for the Rectification of Observed Distributions. *Astronomical Journal*, 79:745, 1974.
- [40] Tim Meinhardt, Michael Moller, Caner Hazirbas, and Daniel Cremers. Learning Proximal Operators: Using Denoising Networks for Regularizing Inverse Imaging Problems. In *Proceedings of the IEEE International Conference on Computer Vision*, pages 1781–1790, 2017.
- [41] Vishal Monga, Yuelong Li, and Yonina C Eldar. Algorithm Unrolling: Interpretable, Efficient Deep Learning for Signal and Image Processing. *IEEE Signal Processing Magazine*, 38(2):18–44, 2021.
- [42] Arkadiĭ Semenovich Nemirovskii and David Berkovich Iŭdin. *Problem Complexity and Method Efficiency in Optimization*. Wiley-Interscience Series in Discrete Mathematics. John Wiley & Sons, Chichester / New York, 1983.
- [43] M. S. Perrin. *Semialgebraic Geometry*. PhD thesis, University of Sydney, 2020.
- [44] Simone Rebegoldi and Luca Calatroni. Scaled, Inexact, and Adaptive Generalized FISTA for Strongly Convex Optimization. *SIAM Journal on Optimization*, 32(3):2428–2459, 2022.
- [45] William Hadley Richardson. Bayesian-Based Iterative Method of Image Restoration. *Journal of the Optical Society of America*, 62(1):55–59, 1972.
- [46] R. Tyrrell Rockafellar. *Convex Analysis*, volume 28. Princeton University Press, 1997.
- [47] Yaniv Romano, Michael Elad, and Peyman Milanfar. The Little Engine That Could: Regularization by Denoising (RED). *SIAM Journal on Imaging Sciences*, 10(4):1804–1844, 2017.
- [48] Leonid I Rudin, Stanley Osher, and Emad Fatemi. Nonlinear Total Variation Based Noise Removal Algorithms. *Physica D: Nonlinear Phenomena*, 60(1-4):259–268, 1992.
- [49] Tim Salimans and Jonathan Ho. Should EBMs Model the Energy or the Score? In *Energy Based Models Workshop-ICLR 2021*, 2021.
- [50] Saverio Salzo and Silvia Villa. Proximal Gradient Methods for Machine Learning and Imaging. *Harmonic and Applied Analysis: From Radon Transforms to Machine Learning*, pages 149–244, 2021.

- [51] Alex Sawatzky, Christoph Brune, Jahn Müller, and Martin Burger. Total Variation Processing of Images With Poisson Statistics. In *International Conference on Computer Analysis of Images and Patterns*, pages 533–540. Springer, 2009.
- [52] Lawrence A Shepp and Yehuda Vardi. Maximum Likelihood Reconstruction for Emission Tomography. *IEEE Transactions on Medical Imaging*, 1(2):113–122, 2007.
- [53] M. Shiota. *Geometry of Subanalytic and Semialgebraic Sets*, volume 150. Springer Science & Business Media, 2012.
- [54] Yu Sun, Brendt Wohlberg, and Ulugbek S Kamilov. An Online Plug-and-Play Algorithm for Regularized Image Reconstruction. *IEEE Transactions on Computational Imaging*, 5(3):395–408, 2019.
- [55] Yu Sun, Zihui Wu, Xiaojian Xu, Brendt Wohlberg, and Ulugbek S Kamilov. Scalable Plug-and-Play ADMM With Convergence Guarantees. *IEEE Transactions on Computational Imaging*, 7:849–863, 2021.
- [56] Marc Teboulle. A simplified view of first order methods for optimization. *Mathematical Programming*, 170(1):67–96, 2018.
- [57] Matthieu Terris, Audrey Repetti, Jean-Christophe Pesquet, and Yves Wiaux. Building Firmly Nonexpansive Convolutional Neural Networks. In *ICASSP 2020-2020 IEEE International Conference on Acoustics, Speech and Signal Processing (ICASSP)*, pages 8658–8662. IEEE, 2020.
- [58] Singanallur V Venkatakrishnan, Charles A Bouman, and Brendt Wohlberg. Plug-and-Play Priors for Model Based Reconstruction. In *2013 IEEE Global Conference on Signal and Information Processing*, pages 945–948. IEEE, 2013.
- [59] Homer F Walker and Peng Ni. Anderson Acceleration for Fixed-Point Iterations. *SIAM Journal on Numerical Analysis*, 49(4):1715–1735, 2011.
- [60] Zhou Wang, Alan C Bovik, Hamid R Sheikh, and Eero P Simoncelli. Image Quality Assessment: From Error Visibility to Structural Similarity. *IEEE Transactions on Image Processing*, 13(4):600–612, 2004.
- [61] Kai Zhang, Wangmeng Zuo, Yunjin Chen, Deyu Meng, and Lei Zhang. Beyond a Gaussian Denoiser: Residual Learning of Deep CNN for Image Denoising. *IEEE Transactions on Image Processing*, 26(7):3142–3155, 2017.
- [62] Richard Zhang, Phillip Isola, Alexei A Efros, Eli Shechtman, and Oliver Wang. The Unreasonable Effectiveness of Deep Features as a Perceptual Metric. In *Proceedings of the IEEE Conference on Computer Vision and Pattern Recognition*, pages 586–595, 2018.
- [63] Zihao Zou, Jiaming Liu, Brendt Wohlberg, and Ulugbek S Kamilov. Deep equilibrium learning of explicit regularization functionals for imaging inverse problems. *IEEE Open Journal of Signal Processing*, 4:390–398, 2023.
- [64] Alessandro Zunino, Marco Castello, and Giuseppe Vicidomini. Reconstructing the Image Scanning Microscopy Dataset: An Inverse Problem. *Inverse Problems*, 39(6):064004, 2023.

A Definition and results in convex/non-convex optimization

In this section, we present the main definitions and results of convex and non-convex optimization, necessary for the understanding of this work. We refer to [7, 8, 38, 50, 56] as standard references on the following concepts.

Notation A.1 (Interior and Closure). *Let $S \subset \mathbb{R}^n$. We denote, respectively, $\text{int}(S)$ the interior of S and \bar{S} the closure of S (w.r.t Euclidean topology).*

Definition A.1 (Domain of a function). *Let $f : \mathbb{R}^n \rightarrow \mathbb{R} \cup \{+\infty\}$. Then $\text{dom}(f) = \{x \in \mathbb{R}^n : f(x) < +\infty\}$.*

Definition A.2 (L -smoothness). *Let $f : \mathbb{R}^n \rightarrow \mathbb{R} \cup \{+\infty\}$. f is said to be L -smooth if:*

- f is differentiable in $\text{int}(\text{dom}(f))$;
- $\exists L > 0 : \|\nabla f(x) - \nabla f(y)\| \leq L\|x - y\| \quad \forall x, y \in \text{dom}(f)$.

Definition A.3 (Legendre function). *Let $h : \mathbb{R}^n \rightarrow \mathbb{R} \cup \{+\infty\}$ be a lower semicontinuous proper convex function. Then h is:*

- (i) *essentially smooth, if h is differentiable on $\text{int}(\text{dom}(h))$, with moreover $\|\nabla h(x^k)\| \rightarrow +\infty$ for every sequence $\{x^k\}_{k \in \mathbb{N}} \subset \text{dom}(h)$ converging to a boundary point of $\text{dom}(h)$ as $k \rightarrow +\infty$;*
- (ii) *of Legendre type if h is essentially smooth and strictly convex on $\text{int}(\text{dom}(h))$.*

Definition A.4 (Bregman divergence). *Given a Legendre function $h : \mathbb{R}^n \rightarrow \mathbb{R} \cup \{+\infty\}$ its associated Bregman distance $D_h : \mathbb{R}^n \times \text{int}(\text{dom}(h)) \rightarrow [0, +\infty]$ is defined in the following way:*

$$D_h(x, y) = h(x) - h(y) - \langle \nabla h(y), x - y \rangle$$

with $x \in \mathbb{R}^n$ and $y \in \text{int}(\text{dom}(h))$. If $x \notin \text{dom}(h)$, then $D_h(x, y) = +\infty \quad \forall y \in \text{int}(\text{dom}(h))$.

Definition A.5 (Bregman Proximal Operator). *Given a Legendre function $h : \mathbb{R}^n \rightarrow \mathbb{R}$ and $\mathcal{R} : \mathbb{R}^n \rightarrow \mathbb{R}$ lower semicontinuous and proper (possibly non-convex), the Bregman Proximal operator of \mathcal{R} (w.r.t h) is defined as follows:*

$$\text{Prox}_{\tau \mathcal{R}}^h(x) = \underset{u \in \mathbb{R}^n}{\text{argmin}} \quad \mathcal{R}(u) + \frac{1}{\tau} D_h(u, x). \quad (\text{A.1})$$

Notice that the operator in (A.1) may be set-valued. A sufficient condition on \mathcal{R} to have (A.1) single-valued is \mathcal{R} being convex and coercive.

Example A.6 (Bregman Proximal operator of $\iota_{[0,a]^n}$ w.r.t $h(x) = -\sum_{i=1}^n \log(x_i)$). *We show here an example of computation of a Bregman Proximal gradient, useful for the aim of this work. By definition we need to solve the following problem:*

$$\text{Prox}_{\tau \iota_{[0,a]^n}}^h(x) = \underset{u \in \mathbb{R}^n}{\text{argmin}} \quad \tau \iota_{[0,a]^n}(u) + D_h(u, x),$$

for some $a > 0$. Now using the definition of D_h and observing that $\iota_{[0,a]^n}(u) = \sum_{j=1}^n \iota_{[0,a]}(u_j)$ we obtain the explicit problem:

$$\underset{u \in \mathbb{R}^n}{\text{argmin}} \quad \sum_{j=1}^n \tau \iota_{[0,a]}(u_j) - \log(u_j) + \log(x_j) + \frac{1}{x_j} (u_j - x_j)$$

Since the function we are minimizing is separable we can solve the problem reasoning on each component. Thus it suffices to solve:

$$\operatorname{argmin}_{u \in \mathbb{R}} \tau_{[0,a]}(u) - \log(u) + \log(x) + \frac{1}{x}(u - x)$$

We write the problem in a constrained form as:

$$u_x^* \in \operatorname{argmin}_{u \in [0,a]} \left\{ D_h(u, x) := -\log(u) + \log(x) + \frac{1}{x}(u - x) \right\}$$

We have to analyze two cases:

-
- if $x > a$, compute $D'_h(\cdot, x)$ the derivative of $D_h(u, x)$ w.r.t the first argument. We get

$$D'_h(u, x) = -\frac{1}{u} + \frac{1}{x} = \frac{u - x}{ux}$$

This derivative is negative in $(0, x)$ and positive in $(x, +\infty)$ and $u = x$ is the global minimum. Thus for $x > a$ the minimum in $[0, a]$ is attained in $u_x^* = a$.

Summarizing

$$\operatorname{Prox}_{\tau_{[0,a]}}^h(x) = \begin{cases} x & \text{if } x \in [0, a] \\ a & \text{if } x > a \end{cases}$$

Finally, we have that:

$$\operatorname{Prox}_{\tau_{[0,a]^n}}^h(x) = \Pi_{[0,a]^n}(x)$$

where Π is the standard Euclidean projection on $[0, a]^n$.

We now recall some definitions and results which will be used to prove convergence of the Mirror Descent algorithm in non-convex setting.

Definition A.7 (Kurdyka-Łojasiewicz property [4]). *A function $f : \mathbb{R}^n \rightarrow \mathbb{R} \cup \{+\infty\}$ is said to have the Kurdyka-Łojasiewicz property at $x^* \in \operatorname{dom}(f)$ if there exists $\eta \in (0, +\infty)$, a neighborhood U of x^* and a continuous concave function $\psi : [0, \eta] \rightarrow \mathbb{R}_+$ such that $\psi(0) = 0$, ψ is C^1 on $(0, \eta)$, $\psi' > 0$ on $(0, \eta)$ and $\forall x \in U \cap \{x \mid f(x^*) < f(x) < f(x^*) + \eta\}$, the Kurdyka-Łojasiewicz inequality holds:*

$$\psi'(f(x) - f(x^*)) \operatorname{dist}(0, \partial f(x)) \geq 1. \quad (\text{A.2})$$

Proper lower semicontinuous functions which satisfy the Kurdyka-Łojasiewicz inequality (A.2) at each point of $\operatorname{dom}(\partial f)$ are called KL functions.

Theorem A.8 ([15]). *Let $f : \mathbb{R}^n \rightarrow \mathbb{R} \cup \{+\infty\}$ be a proper lower semicontinuous, lower bounded function and $a, b, > 0$. Consider a bounded sequence $\{x^n\}_{n \in \mathbb{N}}$ satisfying the following conditions:*

H1 *Sufficient decrease condition: $\forall n \in \mathbb{N}$,*

$$f(x^{n+1}) + a\|x^{n+1} - x^n\|^2 \leq f(x^n).$$

H2 *Relative error condition: $\forall n \in \mathbb{N}$, there exists $\omega_{n+1} \in \partial f(x_{n+1})$ such that*

$$\|\omega_{n+1}\| \leq b\|x^{n+1} - x^n\|.$$

H3 *Continuity condition:* Any subsequence $(x^{k_i})_{i \in \mathbb{N}}$ converging towards \bar{x} verifies

$$f(x^{k_i}) \rightarrow f(\bar{x}) \quad \text{as } i \rightarrow +\infty.$$

If f verifies the Kurdyka–Lojasiewicz property (A.7), then the sequence $\{x^k\}_{k \in \mathbb{N}}$ has finite length, i.e.,

$$\sum_{k=1}^{\infty} \|x^{k+1} - x^k\| < \infty,$$

and it converges to x^* , with x^* a critical point of f .

The preceding theorem does not require the objective function to be convex. For this reason, the Kurdyka–Lojasiewicz property (A.2) is a crucial tool for proving the convergence of schemes within non-convex frameworks. Although the class of functions satisfying this property is broad, direct verification can be challenging. We therefore introduce a class of functions known to satisfy the property of interest, the subanalytic functions.

Definition A.9 (Subanalytic sets and functions). • A subset S of \mathbb{R}^n is a *semianalytic set* if each point of \mathbb{R}^n admits a neighborhood V for which there exists a finite number of real analytic functions $f_{i,j}, g_{i,j} : \mathbb{R}^n \rightarrow \mathbb{R}$ such that

$$S \cap V = \bigcup_{j=1}^p \bigcap_{i=1}^{q_j} \{x \in \mathbb{R}^n \mid f_{i,j}(x) = 0, g_{i,j}(x) < 0\}.$$

- A subset S of \mathbb{R}^n is a *subanalytic set* if each point of \mathbb{R}^n admits a neighborhood V for which

$$S \cap V = \{x \in \mathbb{R}^n \mid (x, y) \in U\},$$

where U is a bounded semianalytic subset of $\mathbb{R}^n \times \mathbb{R}^p$ with $p \geq 1$.

- A function $f : \mathbb{R}^n \rightarrow \mathbb{R} \cup \{+\infty\}$ is called *subanalytic* if its graph

$$\{(x, y) \in \mathbb{R}^n \times \mathbb{R} \mid y = f(x)\}$$

is a subanalytic subset of $\mathbb{R}^n \times \mathbb{R}$.

Lemma A.10 (Stability of subanalytic functions [53]). *The sum of two subanalytic functions is subanalytic if at least one of the two functions maps a bounded set onto a bounded set or if both functions are lower bounded.*

Theorem A.11 (KL property and subanalytic functions [11]). *Let $f : \mathbb{R}^n \rightarrow \mathbb{R} \cup \{+\infty\}$ be a proper, subanalytic function with closed domain and assume that f is continuous on its domain, then f is a KL function.*

We conclude this section presenting two classes of functions which are subanalytic: the analytic and the semialgebraic functions.

Definition A.12 (Real analytic function). *A function $f : A \rightarrow \mathbb{R}$ with $A \subset \mathbb{R}^n$ an open set is said to be (real) analytic at $x_0 \in A$ if there exists a neighborhood U of x_0 such that f can be represented by a convergent power series for all $x \in U$. The function f is said to be analytic if it is analytic at each point of A .*

Definition A.13 (Semialgebraic sets and functions [3]). • A subset S of \mathbb{R}^n is a *real semialgebraic set* if there exists a finite number of real polynomial functions $P_{i,j}, Q_{i,j} : \mathbb{R}^n \rightarrow \mathbb{R}$ such that

$$S = \bigcup_{j=1}^p \bigcap_{i=1}^{q_j} \{x \in \mathbb{R}^n \mid P_{i,j}(x) = 0, Q_{i,j}(x) < 0\}$$

- A function $f : \mathbb{R}^n \rightarrow \mathbb{R} \cup \{+\infty\}$ is called *semialgebraic* if its graph

$$\{(x, y) \in \mathbb{R}^n \times \mathbb{R} \mid y = f(x)\}$$

is a semialgebraic subset of $\mathbb{R}^n \times \mathbb{R}$.

Lemma A.14 (Elementary properties of semi-algebraic sets and functions[36]). *The closure, the interior, and the boundary of a semi-algebraic set are semi-algebraic. Polynomials and indicator function of a semialgebraic set are semialgebraic.*

Lemma A.15 (Stability of semialgebraic class [43]). *The sum, product, and composition of semialgebraic functions are semialgebraic.*

Lemma A.16 ([53]). *Semialgebraic functions and analytic functions with full domain are sub-analytic.*

Note, however, that the trivial extension

$$\tilde{f}(x) = \begin{cases} f(x) & \text{if } x \in A, \\ +\infty & \text{if } x \notin A. \end{cases}$$

to \mathbb{R}^n of an analytic function $f : A \subset \mathbb{R}^n \rightarrow \mathbb{R}$, defined on $A \neq \mathbb{R}^n$, may fail to be subanalytic. As an example, consider $f : (0, +\infty) \rightarrow \mathbb{R}$, defined by $f(x) = \sin\left(\frac{1}{x}\right)$.

An example of function which is analytic on a proper open subset of \mathbb{R}^n with a subanalytic extension is given in Section SM2.2. This shows that the assumption of full domain is sufficient, but not necessary for subanalyticity.

A.0.1 Indicator function of $[0, a]^n$ is KL

Consider, for any $a > 0$, the following function $\iota_{[0, a]^n}$. We start proving that $\iota_{[0, a]^n}(x)$ for $a > 0$ is semialgebraic. From Lemma A.14 it suffices to show that the set $[0, a]^n$ is semialgebraic. We will show that $(0, a)^n$ is semialgebraic and since $[0, a]^n = \overline{(0, a)^n}$ by Lemma A.14 we conclude. For definition A.13 to hold we need to exhibit the polynomials $P_{i,j}$ and $Q_{i,j}$ satisfying the definition. With the following choices:

$$\begin{aligned} P_{i,j}(x) &= 0 \quad \forall i \quad \forall j, \\ Q_{ij}(x) &= x_j(x_j - a) \quad j = 1, \dots, n, \quad i = 1, \end{aligned}$$

we can write:

$$(0, a)^n = \bigcap_{j=1}^n \{x \in \mathbb{R}^n \mid P_{i,j}(x) = 0, Q_{i,j}(x) < 0\},$$

To conclude that $\iota_{[0, a]^n}$ is a KL function, we use Lemma A.16. This lemma implies that the function is subanalytic. We then apply Theorem A.11, as $\iota_{[0, a]^n}$ is continuous on its domain, as per Definition A.1. Since $\iota_{[0, a]^n} = 0 \quad \forall x \in [0, a]^n$, the conclusion follows.

B Proofs of Section 4

In this Section, we report the proofs of Propositions 4.3 and 4.5, and Corollary 4.4. Many of the results presented here are technical extensions of well-known results in non-convex optimization, addressing the validity of the Kurdyka–Lojasiewicz property for subanalytic functions with non-closed domains, as for the KL-dependent functional under consideration. Surprisingly, despite the extensive literature on tailored algorithms for KL minimization in non-convex settings, we could not find any satisfactory result addressing this subtle but crucial technical detail. Clarifying this point not only fills a gap in the existing theory of convergence of non-convex optimization algorithms for such functions, but also strengthens the mathematical foundation of the results presented in the main text.

B.1 Proof of Proposition 4.3

Before proving our main result, we illustrate the need for it with two examples. Consider the functions $\Psi_1, \Psi_2 : \mathbb{R}^2 \rightarrow \mathbb{R} \cup \{+\infty\}$, defined by

$$\Psi_i(x) := \text{KL}(y, A_i x) + \iota_{[0, +\infty)^2}(x), \quad i = 1, 2,$$

where $\iota_{[0, +\infty)^2}$ denotes the indicator function of the nonnegative orthant and the matrices A_i are defined by

$$A_1 = \frac{1}{4}I, \quad A_2 = \begin{bmatrix} \frac{1}{2} & 0 \\ 0 & \frac{1}{2} \end{bmatrix}.$$

In the first case, it is easy to verify that

$$\text{dom}(\Psi_1) = [0, +\infty)^2 \setminus \{(0, 0)\},$$

which is neither closed nor open. In contrast, for the second case,

$$\text{dom}(\Psi_2) = (0, +\infty)^2,$$

which is open. The domain of functions defined in terms of the KL divergence may thus fail to be closed, highlighting the need for Proposition 4.3.

We recall the following result.

Theorem B.1 (Theorem 3.1 [11]). *Let $\Psi : \mathbb{R}^n \rightarrow \mathbb{R} \cup \{+\infty\}$ be a subanalytic function with closed domain, and assume that $\Psi|_{\text{dom} \Psi}$ is continuous. Let $x^* \in \mathbb{R}^n$ be a critical point of Ψ . Then, there exists an exponent $\theta \in [0, 1)$ such that the function*

$$x \mapsto \frac{|\Psi(x) - \Psi(x^*)|^\theta}{m_\Psi(x)}$$

is bounded around x^* , where m_Ψ is defined as

$$m_\Psi(x) := \inf\{\|x^*\| : x^* \in \partial\Psi(x)\} = \text{dist}(0, \partial\Psi(x)),$$

under the convention $m_\Psi(x) = +\infty$ whenever $\partial\Psi(x) = \emptyset$.

In addition we state the following lemma, useful for the proof.

Lemma B.2. *Let $\Psi : \mathbb{R}^n \rightarrow \mathbb{R} \cup \{+\infty\}$ be a subanalytic and coercive function and $K \subset \mathbb{R}$ a compact and subanalytic set. Then $\Psi^{-1}(K)$ is a subanalytic set of \mathbb{R}^n .*

Proof. Before starting we recall standard results on subanalytic sets [10, 37]. In particular given E, F two subanalytic sets of \mathbb{R}^n , then $E \cap F, E \times F$ are subanalytic.

Now we write:

$$\Psi^{-1}(K) = \Pi_{\mathbb{R}^n}(\Gamma_\Psi \cap (\mathbb{R}^n \times K)),$$

where $\Pi_{\mathbb{R}^n} : \mathbb{R}^n \times \mathbb{R} \rightarrow \mathbb{R}^n$, with $\Pi_{\mathbb{R}^n}(x_1, \dots, x_n, x_{n+1}) = (x_1, \dots, x_n)$. Since Ψ is subanalytic, then Γ_Ψ is a subanalytic set of $\mathbb{R}^n \times \mathbb{R}$. Similarly, $\mathbb{R}^n \times K$ is subanalytic, as the Cartesian product of two subanalytic sets. Moreover, $\Gamma_\Psi \cap (\mathbb{R}^n \times K) = \{(x, \Psi(x)) \mid x \in \mathbb{R}^n, \Psi(x) \in K\}$ is bounded since Ψ is coercive, thus it is relatively compact. Finally, note that the function $\Pi_{\mathbb{R}^n}$ is subanalytic, as it is analytic with full domain. To conclude, we use that the image of a relatively compact set by a subanalytic mapping is subanalytic [10, 37], which concludes the proof. \square

We can now prove Proposition 4.3.

Proof. We fix $x^* \in \text{crit}(\Psi)$. By definition $\Psi(x^*) = M < +\infty$. We now divide the proof in two parts:

1. **Part I:** We suppose there exists a compact set D' such that:

- i. $x^* \in D' \subset \text{dom}(\Psi)$;
- ii. there exists a neighborhood U of x^* , s.t. $U \cap \text{dom}(\Psi) \subset D'$;
- iii. D' is a subanalytic set.

We can thus define $\tilde{\Psi} := \Psi + \iota_{D'}$ such that $\text{dom}(\tilde{\Psi}) = D'$. By construction, we show that $\tilde{\Psi}$ satisfies Theorem B.1 at x^* and that there exists a neighborhood of x^* where $\tilde{\Psi} \equiv \Psi$, by which the thesis follows.

2. **Part II:** We show that such D' always exists, providing a constructive way to define it by considering several exhaustive cases.

Part I In order to apply Theorem B.1 we need to show that $\tilde{\Psi}$ is subanalytic and continuous when restricted to its domain. $\tilde{\Psi}|_{D'}$ is continuous, since it holds that $\tilde{\Psi}|_{D'} = \Psi|_{D'}$, where the second function is continuous by hypothesis. In addition D' is closed, since compact. We now show that $\tilde{\Psi}$ is subanalytic. For that, we first show that $\iota_{D'}$ is subanalytic. Since the graph of $\iota_{D'}$ is $\Gamma_{\iota_{D'}} = D' \times \{0\}$ and since cartesian product of subanalytic sets is subanalytic [10, 37], the claim follows. Since Ψ is subanalytic, it follows from Lemma A.10 that the sum $\Psi + \iota_{D'}$ remains subanalytic. We show now that:

$$x \mapsto \frac{|\Psi(x) - \Psi(x^*)|^\theta}{m_\Psi(x)} \quad (\text{B.1})$$

is bounded around x^* . By ii., there exists U neighborhood of x^* , s.t. $U \cap \text{dom} \Psi \subset D'$. Notice that $\forall y \in U \setminus D'$, there holds $\Psi(y) = \tilde{\Psi}(y) = +\infty$. Furthermore, since $U = (U \setminus D') \cup (U \cap D')$ we conclude that Ψ and $\tilde{\Psi}$ coincide on U . By applying Theorem (B.1) to $\tilde{\Psi}$, we conclude that there exists U' neighborhood of x^* , $\theta \in [0, 1)$ and $c > 0$ s.t.

$$\frac{|\tilde{\Psi}(x) - \tilde{\Psi}(x^*)|^\theta}{m_{\tilde{\Psi}}(x)} \leq c$$

for all $x \in U'$. Since $\Psi \equiv \tilde{\Psi}$ on U , then the function defined by (B.1) is bounded in $U \cap U'$. Thus, choosing $\psi := \frac{1-\theta}{c(1-\theta)}$ and choosing $U \cap U'$ as a neighborhood for x^* , we conclude that Ψ satisfies (A.2) at x^* .

Part 2 We start defining $D := \Psi^{-1}((-\infty, M])$, which satisfies i. by definition. Notice that since Ψ is l.s.c., then D is closed and since Ψ is coercive, then D is bounded. Thus D is compact and $x^* \in D$. By definition, there holds $D \cap S = \emptyset$, from which we conclude that $\bar{d} = \text{dist}(D, S) > 0$, where $\text{dist}(D, S)$ denotes the set distance between D and S .

We now aim at finding the required set D' . We observe that there are two possible scenarios:

- $x^* \in \text{int}(D)$: in this case it is possible to find a neighborhood U of x^* s.t. $U \subset D$ and thus trivially $U \cap \text{dom}(\Psi) \subset D$. It thus suffices to pick $D' = D$.
- $x^* \in \partial D$: in this case the existence of such neighborhood is in general false. For instance, if x^* is a global minimizer, then $D = \Psi^{-1}((-\infty, x^*]) = \{x^*\}$. The idea is to define D' by adding points which will allow for finding the desired neighborhood U . To this end, we firstly define the following set:

$$D^\epsilon := \{x \in \mathbb{R}^n \mid \exists y \in D \text{ s.t. } \|x - y\|_2 \leq \epsilon\}.$$

Let us consider $B^\epsilon := D^\epsilon \cap \text{dom } \Psi$. The set B^ϵ is bounded and contained in $\text{dom}(\Psi)$, although, in general, not closed. To bypass the problem, we proceed as follows: we observe that $\text{dist}(B^\epsilon, S) \geq \bar{d} - \epsilon$, thus, taking $\epsilon < \bar{d}$ it holds that $\text{dist}(B^\epsilon, S) > 0$. Thus it follows that $\sup_{x \in B^\epsilon} \Psi(x) = \bar{M}_\epsilon < +\infty$. This leads to $D' = \Psi^{-1}(-\infty, \bar{M}_\epsilon]$, which is a compact contained in $\text{dom}(\Psi)$, hence $B^\epsilon \subset D'$. It thus suffices to consider $U = B_{\frac{\epsilon}{2}}(x^*)$, which by construction is such that $U \cap \text{dom}(\Psi) \subset D'$.

To conclude, it remains to show that in both cases D' is a subanalytic set. Let us observe that D' is given by the following rule $D' = \Psi^{-1}((-\infty, M])$ for some $M \in \mathbb{R}$. Using the fact that Ψ is lower bounded (since it is l.s.c. and coercive), we actually get more precisely that $D' = \Psi^{-1}([-m, M])$, where $m = \inf \Psi$. To conclude, we thus simply apply Lemma B.2 to Ψ and $K = [-m, M]$. \square

B.2 Proof of Corollary 4.4

Proof. The proof consists of checking the validity of the assumptions of Proposition 4.3.

1. Ψ is subanalytic The expression of $\text{KL}(y, Ax)$ is:

$$\text{KL}(y, Ax) = \sum_{i=1}^m y_i \log \left(\frac{y_i}{(Ax)_i} \right) + (Ax)_i - y_i = \sum_{i=1}^m \text{kl}_i(x),$$

where kl_i is the i -th term in the sum defining $\text{KL}(y, A \cdot)$. The idea is to first show that $\widetilde{\text{KL}}_i$ is subanalytic $\forall i = 1, \dots, m$ and then using the stability of the sum of subanalytic functions. Our goal is showing that:

$$\Gamma_{\text{kl}_i} = \{(x, \text{kl}_i(x)) \mid (Ax)_i > 0\} \subset \mathbb{R}^n \times \mathbb{R}$$

is a subanalytic set. In particular, we will prove that it is semianalytic, which implies that it is subanalytic. We firstly show that Γ_{kl_i} is closed. This is true since:

$$\lim_{x \rightarrow z \in \partial \text{dom}(\text{kl}_i)} \text{kl}_i(x) = +\infty.$$

Such property implies that all accumulations points of Γ_{kl_i} belong to Γ_{kl_i} . Once we have this we consider two cases:

- $x \notin \Gamma_{\text{kl}_i}$: in this case it possible to find a neighborhood V of x such that $V \cap \Gamma_{\text{kl}_i} = \emptyset$. Thus, the condition is trivially satisfied.
- $x \in \Gamma_{\text{kl}_i}$: in this case we consider $V = \mathbb{R}^n \times \mathbb{R}$ and we consider $f, g : \mathbb{R}^n \times \mathbb{R} \rightarrow \mathbb{R}$ defined by:

$$\begin{aligned} f(x, t) &:= \left(\frac{(Ax)_i}{y_i} \right)^{y_i} \exp(y_i - (Ax)_i) - \exp(t), \\ g(x, t) &:= -(Ax)_i \end{aligned}$$

under the convention $\left(\frac{(Ax)_i}{0} \right)^0 = 1$. The functions f, g are real-analytic as sum, composition and product of analytic functions. In addition, it holds that:

$$\Gamma_{\text{kl}_i} \cap V = \Gamma_{\text{kl}_i} = \{x \in \mathbb{R}^n \times \mathbb{R} \mid f(x, t) = 0, g(x, t) < 0\}.$$

This shows the semianalyticity of Γ_{kl_i} and thus the claim. To conclude we observe that kl_i is non-negative for all $i = 1, \dots, m$ and thus the sum is still subanalytic (Lemma A.10).

Next, note that given $a > 0$, the function $\iota_{[0,a]^n}(x)$ is semialgebraic, as we showed in Section A.0.1.

To conclude we draw some considerations on R_θ . A neural network consists in the composition of linear functions (which are analytic) and non-linear activation functions. We focus on the particular case where the activation function is the Softplus $\beta(x) = \frac{1}{\beta} \log(1 + \exp(\beta x))$, with $\beta > 0$. This function is analytic for any $\beta > 0$, being it the composition and sum of analytic functions. Thus, a network with softplus as activation functions is analytic (in particular subanalytic as stated in Lemma A.16), as composition and sum of analytic functions with full domain. Hence R_θ is subanalytic and all the three functions considered are subanalytic. To conclude, we need to check if the sum of these three functions is subanalytic, which in general is not true. We proceed as follows:

- (1) $\text{KL}(y, A \cdot) + \iota_{[0,a]^n}$ is subanalytic by Lemma A.10 since both functions are subanalytic and non-negative.
- (2) $R_\theta(K)$ is compact for every compact $K \subset \mathbb{R}^n$ since $R_\theta(x)$ is differentiable on \mathbb{R}^n , hence in particular continuous. Thus R_θ maps bounded sets in bounded sets.
- (3) by Lemma A.10, $(\text{KL}(y, A \cdot) + \iota_{[0,a]^n}) + R_\theta$ is subanalytic as sum of two subanalytic with at least one mapping bounded sets to bounded sets.

2. Ψ is l.s.c. and continuous on its domain The function Ψ is the sum of three l.s.c. functions. Moreover, $\Psi = \text{KL}(y, A \cdot) + R_\theta$ on its domain, which is continuous.

3. Ψ is coercive This holds since $\Psi = +\infty$ in $\mathbb{R}^n \setminus [0, a]^n$.

4. S is closed The set S can be explicitly defined in this case. Let us start by observing that $\text{dom}(\Psi) = [0, a]^n$. Given $x \in [0, a]^n$, we trivially observe that $\Psi(x) = +\infty$ if Ax has at least one 0 component. By now considering the operator $A_i : \mathbb{R}^n \rightarrow \mathbb{R}$, defined by $A_i(x) := \langle a_i, x \rangle$, with a_i being the i -th row of A , we consider $K_i = \ker(A_i)$. We observe that

$$Ax \text{ has at least a 0 component} \iff x \in \bigcup_{i=1, \dots, n} K_i.$$

Thus, S can be written as $S = \left(\bigcup_{i=1, \dots, n} K_i \right) \cap [0, a]^n$. We have that S is closed as the intersection of a closed set with a finite union of closed sets. \square

Remark B.3. *Although $\text{KL}(y, A \cdot)$ is analytic, there holds*

$$\text{dom}(kl_i) = \{x \in \mathbb{R}^n \mid (Ax)_i > 0\},$$

which is not the full space \mathbb{R}^n , so this property cannot be used to prove subanalyticity as a direct consequence. This is why in the proof we directly rely on Definition A.9 showing that its graph is semianalytic, which is not straightforward. A natural attempt would be to consider an analytic function whose zero level set represents the graph of such function, for instance

$$f(x, t) := \text{KL}(y, Ax) - t.$$

However, this function is analytic only on a proper open subset of $\mathbb{R}^n \times \mathbb{R}$, since the KL divergence is not defined everywhere. Therefore, f does not have full domain, whereas Definition A.9 requires the defining function to be analytic on all of $\mathbb{R}^n \times \mathbb{R}$. A different argument is thus needed to establish the semianalyticity of the graph.

B.3 Proposition 4.5

Proof. Proposition 4.5 is a corollary of Theorem 1 of [29]. In particular we need to prove the following facts:

- (i) $h : \mathbb{R}^n \rightarrow \mathbb{R} \cup \{+\infty\}$ defined in (3.2) is of Legendre-type and strongly convex on any bounded convex subset of its domain.
- (ii) $F := \text{KL}(y, A\cdot) + R_\theta$ is proper, C^1 on $\text{int}(\text{dom}(h))$, with $\text{dom}(h) \subset \text{dom}(F)$.
- (iii) $\mathcal{R} := \iota_{[0,a]^n}$ is proper, lower semicontinuous with $\text{dom}(\mathcal{R}) \cap \text{int}(\text{dom}(h)) \neq \emptyset$.
- (iv) $\Psi := F + \mathcal{R}$ is lower-bounded, coercive and verifies the Kurdyka-Łojasiewicz property.
- (v) For $x \in \text{int}(\text{dom}(h))$,

$$T_\tau(x) = \underset{x \in \mathbb{R}^n}{\text{argmin}} \mathcal{R}(x) + \langle x - x^k, \nabla F(x^k) \rangle + \frac{1}{\tau} D_h(x, x^k)$$

is nonempty and included in $\text{int}(\text{dom}(h))$.

- (vi) There is $L > 0$ such that, $Lh - F$ is convex on $\text{Conv}(\text{dom}(\mathcal{R})) \cap \text{int}(\text{dom}(h))$.
- (vii) For all $\alpha > 0$, ∇h and ∇F are Lipschitz continuous on $\{\Psi(x) \leq \alpha\}$.

We show only the points that are not straightforward. This proof is based on Section E.3 of [29]. However, in Section B.3.3, we establish the assumption using a general argument, rather than one tailored to the specific choice of h .

B.3.1 Assumption (iv): properties on $\Psi = \text{KL}(y, A\cdot) + R_\theta + \iota_{[0,a]^n}$

These properties were already proved in B.2.

B.3.2 Assumption (v): well-posedness

We recall the definition of T_τ , for $k \geq 0$ and for a given $x^k \in \text{int}(\text{dom}(h))$:

$$T_\tau(x^k) \in \underset{x \in \mathbb{R}^n}{\text{argmin}} \mathcal{R}(x) + \langle x - x^k, \nabla F(x^k) \rangle + \frac{1}{\gamma} D_h(x, x^k).$$

Using the definition of $D_h(\cdot, \cdot)$ (A.4) and omitting all terms that do not depend on x , we consider the following function:

$$\beta(x) = \mathcal{R}(x) + \langle x, \nabla F(x^k) \rangle + \frac{1}{\gamma} (h(x) - \langle \nabla h(x^k), x \rangle)$$

Since $\mathcal{R} = \iota_{[0,a]^n}$ is convex and h is strictly convex then β is strictly convex, thus its set of minimizers is empty or single-valued. In addition, β is equal to $+\infty$ in $\mathbb{R}^n \setminus [0, a]^n$, hence it is coercive. Thus β admits a unique global minimiser that belongs to $[0, a]^n$. To conclude observe that $\beta = +\infty$ on the boundary of $[0, a]^n$, since $h(x) = +\infty$ if $x \notin \mathbb{R}_{++}^n$ and the other terms are bounded in $[0, a]^n$. Thus the minimiser must belong to $(0, a)^n \subset \text{int}(\text{dom}(h))$, as β is proper.

B.3.3 Assumption (vi): NoLip

$\text{KL}(y, A_\cdot)$ satisfies NoLip property w.r.t Burg's entropy (3.2) with $L \geq \|y\|_1$ [6]. Thus it remains to prove that:

$$\exists L' > 0 \text{ such that } L'h - R_\theta \text{ is convex on } \text{Conv}(\text{dom}(\mathcal{R})) \cap \text{int}(\text{dom}(h)) = (0, a]^n.$$

This is indeed a sufficient condition showing the existence of an $\tilde{L} > 0$ satisfying NoLip property (Definition 4.1 of the main text) for the composite functional, simply by choosing $\tilde{L} = L' + L$. In fact, $\tilde{L}h - (\text{KL}(y, A_\cdot) + R_\theta) = (Lh - \text{KL}(y, A_\cdot)) + (L'h - R_\theta)$. Since the sum of convex functions is convex, this proves the desired property. To show the existence of such a L' , given the regularity of h and R_θ it is enough to show that [6]:

$$\exists L' > 0 \text{ s.t. } L'\nabla^2 h(x) - \nabla^2 R_\theta(x) \succeq 0, \forall x \in \text{Conv}(\text{dom}(\mathcal{R})) \cap \text{int}(\text{dom}(h)).$$

We start observing that both h and R_θ are C^2 functions, thus their Hessians are symmetric (on every point) for Schwarz's Theorem. In addition, for the real spectral Theorem $\nabla^2 h(x)$ and $\nabla^2 R_\theta(x)$ have real eigenvalues $\forall x \in \mathbb{R}_{++}^n$. We want to show then that:

$$\exists L' > 0 \text{ such that } \inf_{x \in (0, a]^n} \min \lambda(L'\nabla^2 h(x) - \nabla^2 R_\theta(x)) \geq 0$$

where by $\lambda(\cdot)$ we denote the spectrum of a matrix. To show such property, we need the following result:

Lemma B.4. *Let C, D be real symmetric matrices. Let λ^- and λ^+ the minimum and maximum eigenvalue of C , and μ^- and μ^+ respectively for D . Then, calling γ^- and γ^+ the minimum and maximum eigenvalue of $C + D$ there holds:*

$$\lambda^- + \mu^- \leq \gamma^- \leq \gamma^+ \leq \lambda^+ + \mu^+.$$

Proof. We prove only: $\lambda^- + \mu^- \leq \gamma^-$, since the proof of the other inequality is similar. We know:

$$\lambda(C) \subset [\lambda^-, \lambda^+], \quad \lambda(D) \subset [\mu^-, \mu^+].$$

Thus

$$\lambda(C - \lambda^- I) \subset [0, \lambda^+ - \lambda^-], \quad \lambda(D - \mu^- I) \subset [0, \mu^+ - \mu^-].$$

Therefore $C - \lambda^- I$ and $D - \mu^- I$ are positive semi-definite. Thus $(C - \lambda^- I) + (D - \mu^- I) = (C + D) - (\lambda^- + \mu^-)I$ is positive semi-definite, since sum of positive semi-definite matrices is positive semi-definite.

The latter implies:

$$\lambda((C + D) - (\lambda^- + \mu^-)I) \subset [0, +\infty].$$

We conclude observing that

$$C + D = (C + D) - (\lambda^- + \mu^-)I + (\lambda^- + \mu^-)I,$$

by which we have that for the spectrum, there holds:

$$\lambda(C + D) \subset [\lambda^- + \mu^-, +\infty.] \quad \square$$

□

To conclude, we have to pay attention to the fact that the Hessian matrices of h and R_θ depend on $x \in \text{int}(\text{dom}(h))$, while, ideally, we would like to get a uniform bound. Since, by

assumption, R_θ is analytic, then R_θ has a Lipschitz gradient (over a compact set), which implies that for $x \in (0, a]^n$:

$$s(x) = \|\nabla^2 R_\theta(x)\| = \max \{ |\min \lambda(\nabla^2 R_\theta(x))|, |\max \lambda(\nabla^2 R_\theta(x))| \} \leq M.$$

On the other side, since h is strongly convex on any bounded and convex set, we have:

$$\inf_{(0, a]^n} \min \lambda(\nabla^2 h(x)) \geq m > 0.$$

Hence, it is thus possible to find $L' > 0$ s.t

$$\inf_{x \in (0, a]^n} \min \lambda(L' \nabla^2 h(x) - \nabla^2 R_\theta(x)) \geq L'm - M \geq 0.$$

□

Observe that this way a proceeding is still true for every Legendre function h that is strongly convex on bounded and convex set and do not use the analytic expression of Burg's entropy. Now the thesis is a direct application of Theorem 1 of [29].

For the sake of completeness we show that, h chosen as the Burg's entropy is strongly convex on bounded and convex set of its domain. Let $B \subset \mathbb{R}_{++}^n$ be a bounded and convex set. By (3.2), it follows that:

$$\nabla^2 h(x) = \text{diag} \left(\frac{1}{x^2} \right), \text{ with } \frac{1}{x^2} = \left(\frac{1}{x_1^2}, \dots, \frac{1}{x_n^2} \right).$$

Since $h \in C^2(\mathbb{R}^n)$, it suffices to show that. there exists $m > 0$ such that:

$$\inf_{x \in B} \min \lambda(\nabla^2 h(x)) \geq m > 0.$$

Since $B \subset \mathbb{R}_{++}^n$ is bounded, then there exists $M > 0$ s.t $B \subset (0, M]^n$ and to conclude we observe:

$$\inf_{x \in B} \min \lambda(\nabla^2 h(x)) \geq \inf_{x \in (0, M]^n} \min \lambda(\nabla^2 h(x)) = \inf_{u \in (0, M]} \frac{1}{u^2} = \frac{1}{M^2} > 0.$$

C Evaluation Metrics

In the main text we consider the three following well-known metrics to evaluate the quality of the reconstructions:

- **PSNR** (Peak Signal-to-Noise Ratio): This metric quantifies the reconstruction quality of an image in terms of pixel-wise similarity. It takes values in decibels (dB), typically ranging from 20 dB to 40 dB for natural images.
- **SSIM** (Structural Similarity Index Measure) [60]: SSIM assesses the structural similarity between two images, considering luminance, contrast, and structure. Its values range between 0 and 1, where 1 signifies perfect similarity and 0 indicates no similarity.
- **LPIPS** (Learned Perceptual Image Patch Similarity) [62]: This metric measures the perceptual distance between two images by utilizing a pre-trained neural network model, which is designed to correlate better with human perception of similarity. It takes positive values, generally close to 0 for very similar images and increasing as dissimilarity grows.

D Pre-training

We consider here DEQ-RED method. We describe in the following a pre-training strategy which could be beneficial for two reasons. Firstly, given that each evaluation of the Deep Equilibrium models considered necessitates convergence, we empirically observed that randomly initialized weights often required a substantial number of iterations to reach a fixed point, translating to increased GPU computational time during the training process. Secondly, considering the non-convex nature of the training objective, a judicious initialization of the network weights can play a crucial role in guiding the optimization process towards more favorable local minima, potentially leading to improved overall performance and a more robust final model. For the reasons, we employed a pre-training strategy. In particular, given $R_\theta(x) = \frac{1}{2}\|x - N_\theta(x)\|^2$ we considered its associated Gradient step denoiser [30] $D_\theta(x) := x - \nabla R_\theta(x)$ and we trained it on Gaussian denoising task. To see the benefits of this pre-training strategy, we considered a small training problem where we simultaneously trained two models: one pre-trained and the other not. The dataset considered was a subset of the dataset proposed in Section 6.1.1, and for the training, we followed the same modalities as in Section 6.1.3 As illustrated in Figure 12, the

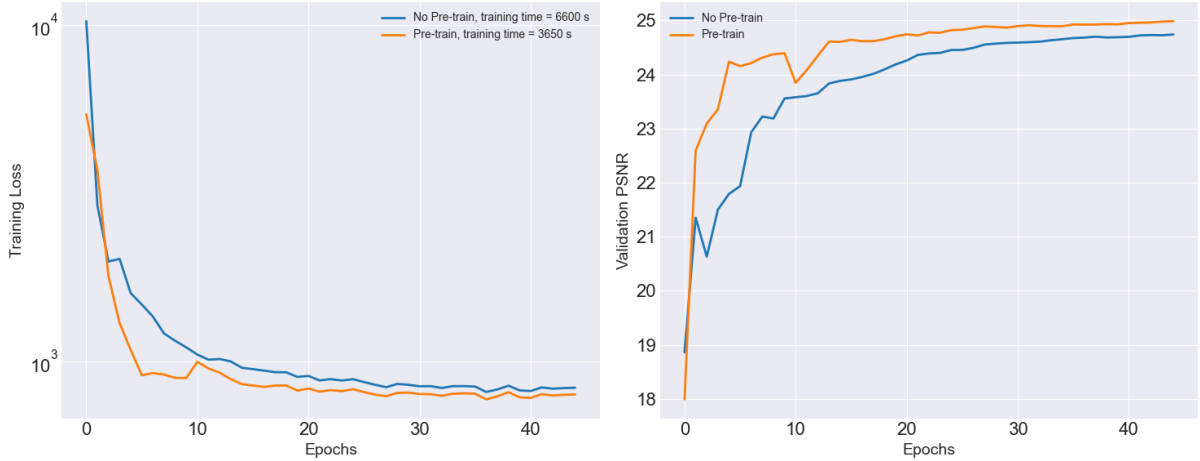


Figure 12: Effect of pre-training for DEQ-RED.

empirical findings unequivocally highlight the advantageous impact of pre-training. This benefit is manifested both in a marked decrease in the computational resources required for training, leading to shorter training durations, and a discernible enhancement in the PSNR metric when evaluated on the validation dataset.